Article type: Full Paper

Multiwall Carbon Nanotubes Covalently Modified by Cobalt (II) Tetraaminophthalocyanines as an Efficient Sulfur Redox Catalyst for High-performance Lithium-Sulfur Batteries

*Xiao-Xia Yang, Wen-Zheng Du, Xu-Ting Li, Yang Zhang, Zhao Qian, Mark James Biggs and Cheng Hu**

X. X. Yang, W. Z. Du, X. T. Li, Y. Zhang, Z. Qian, C. Hu
Key Laboratory for Liquid-Solid Structural Evolution and Processing of Materials (Ministry of Education), School of Materials Science and Engineering
Shandong University
Ji'nan 250061, Shandong, P.R. China
E-mail: c.hu@sdu.edu.cn

M.J. Biggs
College of Science and Technology
Nottingham Trent University
Nottingham NG11 8NS, United Kingdom

Keywords: lithium−sulfur batteries, sulfur redox catalyst, covalent modification, cobalt (II) tetraaminophthalocyanine, multiwall carbon nanotubes.

An efficient Li-S redox catalyst of MWCNTs covalently modified by cobalt (II) tetraaminophthalocyanines (TaPcCo-MWCNTs) is reported. Effective lithium polysulfide (LiPS) capturing is enabled by the lithiophilic N-containing phthalocyanine rings and the sulfiphilic Co central atoms. This adsorption geometry utilizes the Co unoccupied d-orbitals as electron superexchange highways. Elevated kinetics of LiPSs reactions in the liquid phase as well as liquid-solid transitions are revealed by electrochemical measurements and density functional theory calculations. Uniform deposition of Li_2S films is also observed that preserves cathode integrity and sulfur utilization during cell cycling. The catalysed sulfur redox is also greatly facilitated by the fast electron and Li-ion transport to and from the reaction sites *via* the conductive MWCNT skeletons and the lithiophilic substituent amino groups on TaPcCo. With 6 wt% addition of TaPcCo-MWCNT in the cathode coatings, high sulfur utilization is achieved with areal sulfur loadings up to 7 mg cm^{-2}. Stable long-term cycling is achieved at 1C under 5 mg cm^{-2} of sulfur loading, with an initial areal capacity of 4.4 mAh cm^{-2} and a 500-cycle retention of 3.5 mAh cm^{-2}. Considering the high structural diversity of phthalocyanines macromolecules, this study offers opportunities for a new class of Li-S catalysts.

1. Introduction

The pressing environmental crisis is driving a global clean-energy revolution, bringing with it fast-rising standards for electrical energy storage devices. Lithium-sulfur (Li-S) batteries are among the most promising candidates of next-generation secondary batteries owing to their high theoretical energy density (2600 Wh kg^{-1}) enabled by the multi-electron electrochemical redox reaction between lithium metal and low-cost and environment-friendly elemental sulfur.[1] The Li-S reaction chemistry requires effective electrode design to realize high energy storage performance in practical cells. Sulfur undergoes solid-liquid-solid transitions during charge/discharge, with sulfur and its fully discharge product Li_2S in the solid phase and both possessing low electrical and Li-ion conductivities.[2] The difference of sulfur and Li_2S in density results in a significant volume change during charge/discharge, applying periodic stress and strain that challenges the integrity of the cathode and the entire cell.[3] Although conductive carbon current-collecting matrixes are widely employed,[4] high sulfur utilization is typically difficult to achieve. Sulfur and Li_2S are intermediated by a sequence of lithium polysulfides (LiPSs) with sluggish conversion kinetics.[5] Dissolution of LiPSs also leads to a loss of active materials and a resulting "shuttle effect" that reduces coulombic efficiency and shortens cell cycle life.[6] The above issues become particularly acute at practical extremes of areal sulfur loadings, which are critical for future large-scale implementation of Li-S batteries.[7]

Proper management of cathode sulfur-containing active materials plays a key role in addressing the above technical issues. To achieve better affinity of the LiPSs with conductive carbons, efforts have been devoted to chemically immobilizing LiPSs *via* polar-polar interactions.[8] Metal compounds offering superior polarity and high LiPSs chemisorption potentials (*e.g.* oxides,[9]

hydroxides,[10] nitrides,[11] sulfides,[12] phosphides,[13] carbides[12a, 14] and metal-organic frameworks[15]) have been introduced to Li-S cathodes to efficiently capture LiPSs and suppress the "shuttle effect". Saturation of surface adsorption sites is, however inevitable especially at high sulfur loadings, leading to uncontrolled LiPSs dissolution and reduced sulfur utilization. Promoting the subsequent redox reaction of adsorbed LiPSs is therefore highly desirable to achieve stable cycling of high loading Li-S cells. Owing to the presence of incompletely filled d-orbitals, many of the above mentioned inorganic transition metal (Fe, Co, Ni *etc*.) compounds exhibit outstanding catalytic effects on the Li-S chemistry.[16] Screening proper catalysts to enable fast sulfur redox kinetics in the liquid phase as well as smooth and even deposition/decomposition of S and Li_2S in the liquid-solid phase transitions have recently become a focused research area of the Li-S advancement.[16b]

Effective catalysts promote the Li-S redox kinetics by elevating the electron exchange between donors and acceptors in the electrochemical reaction system. Design of a high efficiency cathode catalytic material should take into account the following three principles. First, maximize the exposure of catalytic-active sites to enable satisfying regulation of sulfur redox at a moderate loading amount. This can be achieved by reducing the dimensions of catalytic materials, as shown on few-layered MoS2 and WS_2 nanosheets by the Manthiram[12b] and Arava[17] group, respectively. Second, facilitated conversion of LiPSs in the liquid phase as well as during the liquid-solid transitions of active sulfur species.[18] Third, high intrinsic electrical conductivity that enables fast electron and Li-ion transports to support continuous electrochemical sulfur redox. Metal carbides,[19] nitrides,[20] and phosphides[21] exhibit metal-like high electrical conductivity and

heterostructures such as TiO_2–TiN[22] and VO_2–VN[23] have therefore been proposed to bring together the merits of strong LiPSs chemisorption with high electrical conductivity.

Following the above three principles, this study reports a Li-S redox catalyst based on multiwall carbon nanotubes (MWCNTs) that are chemically modified by cobalt (II) tetraaminophthalocyanines (TaPcCo), which demonstrates unique advantages over other transition metal compounds. Metal phthalocyanines (MPc) are 18π conjugated metal-N_4 macrocycles possessing wide applications and outstanding catalytic effects in various chemical processes.[24] CoPc particles physically loaded on a carbon support has been demonstrated as an effective Li-S redox promotor,[25] whilst other metal organic macromolecules such as porphyrins have also been employed as sulfur redox catalysts.[26] A mechanism study of MPc catalysed Na pentasulfide reduction reveals that catalysis is enabled by the electron superexchange tunnelling between the conductive carbon surface and pentasulfide ions *via* d-orbital vacancies in the central metal atom.[26a] This suggests that the proper nano-structuring of MPcs with the conductive carbon substrate plays a significant role in the final catalysis efficiency. MPcs can be substituted with various functional groups to offer a wide range of LiPSs affinity and improved processability for catalyst nano-structuring. Tetra-amino substituents are utilized herein to enable covalent linkages to MWCNTs *via* secondary amine bridges, whilst the remaining amino groups facilitate Li-ion diffusion through strong coordination interactions.[27] The prepared TaPcCo-MWCNT possesses a carbonaceous core with good electrical conductivity and a few-nm thick surface layer of covalently bonded and well exposed TaPcCo to provide abundant sulfiphilic (S-Co) and lithiophilic (Li-N) binding sites. At a moderate loading amount (6 wt%) in the cathode coatings, TaPcCo-MWCNT effectively promotes sulfur redox kinetics whilst enabling smooth deposition and decomposition

of Li_2S. Significantly improved sulfur utilization is achieved at C rates ranging from 0.2C (1398 mAh g^{-1}) to 4C (614 mAh g^{-1}). High specific capacities and stable cycling of high areal sulfur loading cathodes (5 mg cm^{-2}) are also demonstrated with TaPcCo-MWCNT at 0.5C and 1C. Detailed working mechanism of the TaPcCo-MWCNT catalytic material is further revealed by electrochemical measurements and density functional theory (DFT) calculations.

2. Results and Discussion

Synthesis and structural representations of TaPcCo-MWCNT and the cathode composite are schematically illustrated in **Figure 1** (details in the Experimental Section). As shown in Figure 1a**,** TaPcCo was synthesised following the well-established procedure of Achar *et. al.*.[28] Cobalt tetranitrophthalocyanine (TnPcCo) was first prepared by heating and refluxing 4-nitrophthalic anhydride (4-NPA, precursor), urea (nitrogen source) and cobalt chloride hexahydrate (cobalt source) in nitrobenzene. TaPcCo was subsequently obtained by further refluxing TnPcCo with sodium sulfide nonahydrate (reductive agent) to transfer the nitro-groups into amino-groups. Molecular fingerprints of synthesized TnPcCo and TaPcCo were confirmed by Fourier-transform infrared spectroscopy (FTIR) (Figure S1, Supporting Information, SI). Chemical modification of MWCNT with TaPcCo was achieved *via* the pyridine catalysed reaction between fluorinated MWCNT (F-MWCNT) and TaPcCo,[29] where amino-groups substitute fluoro-groups to form -NH- covalent bonds between the phthalocyanine (Pc) complexes and the MWCNT skeletons (Figure 1b-c). The models used here are only for a representative purpose as the following TEM results suggest a more amorphous nature of the MWCNT core. The lithiophilic N-containing Pc ring and the sulfiphilic Co central atom together provide high LiPSs affinity. The well-exposed Co atom in the TaPcCo-MWCNT structure also acts as a superexchange electron highway that enables

catalysed transformation of polysulfide anions, which are effectively captured by the Co atom *via* a S-Co bond formed on the terminal S atom (Figure 1d). The TaPcCo content in TaPcCo-MWCNT was determined to be around 50 wt% by the difference in mass between collected TaPcCo-MWCNT and F-MWCNT (F content discounted). TaPcCo-MWCNT was uniformly loaded into a 3D network of carbon nanofibers (TaPcCo-MWCNT/CNF) at the mass ratio of 3:7, which all together serve as the skeleton matrix of a 75 wt% sulfur loading cathode composite (TaPcCo-MWCNT/CNF/S, Figure 1e). This results in 60 wt% of sulfur loading in the cathode coatings and corresponding contents of TaPcCo-MWCNT in the cathode coatings as low as c.a. 6 wt%.

X-ray diffraction (XRD) was carried out for phase identification of the prepared TaPcCo-MWCNT. As shown in **Figure 2**a, two broad diffraction peaks centred at 2θ of 13° and 42° are observed on F-MWCNT, correlating respectively to the planar (001) reflection and in-plane C–C (100) reflection that are typically observed on carbon monofluorides.[23] Diffraction peaks from prepared TaPcCo are in good agreement with β-form cobalt phthalocyanine (JCPDS File Card No.14-0948) owing to the fact that the crystalline structure is not altered by amino substituents at 2, 9, 16, 23 positions.[30] The F-MWCNT (001) peak is absent from TaPcCo-MWCNT, whilst a diffusing diffraction peak centred at 2θ of 23° is observed and can be assigned to planar (002) reflection of graphitic carbons. Diffraction peaks of TaPcCo are also not observed from TaPcCo-MWCNT, indicating the absence of crystalline TaPcCo in the covalent modification structure.

FTIR was performed on TaPcCo-MWCNT and compared with the results from F-MWCNT and TaPcCo, the obtained spectra are shown in Figure 2b. The spectrum of TaPcCo-MWCNT exhibits characteristic bands of TaPcCo, originated from the stretching vibration of C=N (c.a. 1640-1690 cm^{-1}),[31] C-N (c.a. 1020-1250 cm^{-1}),[32] -NH_2 (c.a. 3500 cm^{-1}),[33] as well as the conjugated

Pc ring (c.a. 745 cm^{-1}).[29] The absorption band at 1213 cm^{-1}, which originates from the C-F bonds in F-MWCNT,[34] disappears from the spectrum of TaPcCo-MWCNT. This indicates the complete removal of the fluoro-groups and is in line with the XRD results. A newly-formed absorption band at 3322 cm^{-1} is found in the spectrum of TaPcCo-MWCNT, which can be assigned to secondary amine C-NH-C bonds[35] that act as covalent connections between the TaPcCo molecules and the MWCNT skeletons.

Chemical bonding information of TaPcCo-MWCNT were further analysed using X-ray photoelectron spectroscopy (XPS). The survey spectrum (Figure S2, SI) exhibits the absence of a F1s peak, which indicates the complete removal of fluorine. The elemental compositions of C, N, and Co were calculated to be 77.5 at%, 20.8 at% and 1.7 at% respectively. The atomic N:Co ratio (12.23:1) agrees well with the molecular formula of TaPcCo ($C_{32}N_{12}H_{20}Co$). However, the measured C:N ratio is lower than the actual value as XPS probes only around 20 nm into the sample and TaPcCo exists mainly on the external surface. The atomic C:N ratio was further determined using CHN elemental analysis to be 7.18:1. Since the atomic C:N ratio in TaPcCo is 2.67:1, the extra C can be attributed to MWCNT and this gives an estimated mass ratio of MWCNT:TaPcCo close to 1:1.

The high-resolution C1s and N1s spectra of TaPcCo-MWCNT are deconvoluted and presented in Figure 2c-d. The peak located at 284.85 eV with the highest intensity in the C1s spectrum can be attributed to sp^2 hybridized C-C bonds in the MWCNT skeleton.[36] Peaks associated with C=N-C in the Pc ring (C1s 284.7 eV and N1s 397.88 eV),[37] primary amines C-NH_2 of TaPcCo (C1s 287.79 eV and N1s 399.41 eV),[38] as well as the newly-formed bridging secondary amines C-NH-C (C1s 286.2 eV and N1s 398.87 eV)[32] are all well resolved. The areal ratio of peaks assigned to

free -NH_2 and bridging C-NH-C are calculated to be close to 3:1 in both the C1s and N1s spectra, which confirms the designed structure of the chemically linked TaPcCo molecules shown in Figure 1. In addition, the calculated ratio of ammonia nitrogen (C-NH-C plus C-NH2) to phthalocyanine nitrogen (C=N-C) is close to 1:2, which is consistent with the structure of TaPcCo. The N-metal interactions are typically not resolved in the N1s spectrum,[39] therefore a N-Co peak was not deconvoluted. The azo (outer) and pyrrolic (inner) N atoms on the Pc ring are only separated by 0.3 eV on the N1s spectrum,[39b] and they are deconvoluted to one peak as C=N-C in the spectrum. The high resolution Co2p spectrum (Figure 2e) is composed of two peaks at 795.3 eV and 779.7 eV with associated satellites corresponding to $Co2p_{1/2}$ and $Co2p_{3/2}$ respectively, indicating the presence of Co^{2+}. The shoulder at 781.81 eV on the $Co2p_{3/2}$ peak can be assigned to the Co-N interactions with the pyrrolic N atoms on the Pc ring.[40] The XPS and FTIR results, especially the characteristic features of the C-NH-C secondary amines formed from the chemical modification, confirm the as-designed chemical structure of TaPcCo-MWCNT.

Raman spectroscopy was performed on F-MWCNT and TaPcCo-MWCNT, the results are shown in Figure 2f. F-MWCNT does not exhibit any outstanding features from 600 to 2200 cm^{-1} due to the loss of sp^2 hybridized local structure.[29, 34a] The Raman spectrum of TaPcCo-MWCNT presents sharp D, G, and D' and TPA bands that indicates a well-defined sp^2 hybridized carbon structure restored during the synthesis.[41] The peak sharpness is comparable with carbons obtained from high carbonization temperatures and the I_D/I_G ratio is calculated to be 2.6.[41] As evidenced by the XPS and FTIR results, F atoms were complete removed during the synthesis of TaPcCo-MWCNT. However, as suggested by the following TEM measurements, the substitution by TaPcCo molecules mainly exist on the external surface of the MWCNT. Within the MWCNT core,

the Raman results indicate the restoration of the carbon sp^2 ordering in short- and medium-range. This is supported by the strong C-C sp^2 feature observed on the XPS C1s spectrum as well as the formation of a broad and outstanding carbon (002) peak on the XRD result. Carbonaceous (002) fringes with a sp^2 nature are also well-resolved in the TEM images.

Surface morphologies of TaPcCo-MWCNT and F-MWCNT were investigated by scanning electron microscopy and the results are shown in Figure S3 (SI). Compared with F-MWCNT prior to chemical modification, TaPcCo-MWCNT exhibits a rough surface morphology of chemically decorated TaPcCo and no precipitates of physically loaded TaPcCo are visible. Transmission electron microscopy (TEM) was further employed to examine the microstructure. TEM images of F-MWCNT (**Figure 3**a) and TaPcCo-MWCNT (Figure 3b) at low magnifications are consistent with the SEM observations, whilst the rough periphery of chemically decorated TaPcCo is better resolved. This microstructure of TaPcCo-MWCNT maximizes the exposure of active binding and catalytic sites, which facilitates LiPSs adsorption and their catalysed electrochemical transformation as demonstrated in the following sections. The high-resolution TEM image of TaPcCo-MWCNT in Figure 3c reveals its structural integrity and uniformity. The diffuse rings in the selected area electron diffraction (SAED) pattern inset to Figure 3c indicate the presence of short-range sp^2 C-C ordering in the MWCNT core, which agrees with the XRD result from bulk sampling. A close-up of its periphery (Figure 3d) suggests the existence of an external amorphous TaPcCo modified layer forming a smooth interface with the highly carbonized MWCNT skeleton. The thickness of this modified layer varies from around 3.5 nm to 6 nm on different observation positions (Figure 3d and Figure S6 in SI). Given that the in-plane diagonal length of TaPcCo is 1.72 nm (marked in Figure 1b), it is reasonable to infer that the external 2-3 layers of the MWCNT

are modified with TaPcCo molecules. The clearly observed carbon (002) lattice fringes on the MWCNT core indicate good electrical conductivity to the active sites on the bonded TAPcCo, which together provide a synergic promotion to the Li-S electrochemical redox. The observed curvatures on the (002) fringes originate from the presence of point-defects formed at the relatively low synthesis temperature and is in-line with the Raman spectroscopy results. The uniform microstructure of TaPcCo-MWCNT is further evidenced by the high-angle annular dark-field (HAADF) image in Figure 3e. Corresponding energy dispersive X-ray spectroscopy (EDX) elemental mapping illustrates the homogeneous distributions of C, N and Co (Figure 3f-h), which results from the chemical modification method as compared with physical counterparts.

The chemical linkage between TaPcCo and MWCNT ensures its preservation in the cathode and high utilization for the catalysis of sulfur redox that involves solid-liquid transitions. TaPcCo is highly soluble in the ether-based electrolyte of Li-S batteries. This is reflected by the strong colour change of the DME/DOL solvent to dark green due to the dissolution of TaPcCo (Figure S3, SI). The colourless DME/DOL solvent with soaked TaPcCo-MWCNT indicates no loss of TaPcCo into the electrolyte from the cathode (Figure S4, SI). The stable chemical linking between TaPcCo and MWCNT is also confirmed by the subtle weightloss of TaPcCo-MWCNT up to 400 °C from the thermogravimetric analysis (TGA) result in N_2 (Figure S5, SI).

To characterize the sulfur redox mechanism at the presence of TaPcCo-MWCNT, cyclic voltammetry (CV) was performed on symmetric cells composed of identical TaPcCo-MWCNT/CNF electrodes or pure CNF electrodes from -1 to 1 V at a scan rate of 3mV s^{-1}. The electrolyte contains 0.2 M Li_2S_6 and the measured current is normalized to the cell sulfur content. As shown in **Figure 4**a, the CV profile of the TaPcCo-MWCNT cell exhibits four distinct peaks

with high reversibility, forming two redox pairs representing the solid-liquid-solid transitions of Li_2S–$Li2S_6$ (a/b) and Li_2S_6-S (c/d).[9b] In contrast, the CV profile from pure CNF symmetric electrodes shows diffusing anodic and cathodic peaks with much lower current densities. Reduced overpotentials on both redox pairs (a/b: ±0.1 V *vs* ±0.13 V; and c/d: ±0.32 V vs ±0.6 V) are revealed for electrodes containing TaPcCo-MWCNT, which clearly demonstrates the significantly improved electrochemical conversion kinetics.

CV tests were also conducted on Li-S full cells to investigate the overall electrochemical characteristics with and without TaPcCo-MWCNT in the cathodes. Profiles at the scan rate of 0.1 mV s^{-1} are shown in Figure 4b. Two oxidation and reduction pairs are clearly observed from the cell with TaPcCo-MWCNT added in the cathode. The cathodic peaks at 2.319 V and 2.043 V originate from the reduction of sulfur to long-chain LiPSs and the consecutive conversion to Li_2S *via* short-chain polysulfides, respectively. These are consistent with the two discharge plateaus obtained in the galvanostatic discharge profiles (**Figure 5**b). In the anodic sweep, the major peak at 2.368V with a shoulder at 2.403V can be attributed to the reverse oxidation of Li_2S to long-chain LiPSs, short-chain LiPSs and ultimately sulfur, agreeing with the two charge plateaus in the galvanostatic charge profiles (Figure 5b). Compared with pure CNF, the CV profile with TaPcCo-MWCNT exhibits a negative shift of the major anodic peak as well as positive shifts of both cathodic peaks, resulting in a significant decrease in the potential difference ΔV (0.325 V *vs* 0.425 V) and the charge/discharge overpotential. The significant improvements in current densities of all CV peaks also indicate enhanced sulfur utilization.

Additional CV tests were performed on Li-S full cells at elevating scan rates up to 1 mV s^{-1} to investigate the cathode responses at fast potential changes. As shown and compared in Figure 4c-

d, CV profiles from the cell with TaPcCo-MWCNT added in the cathode maintain the original shape and exhibit significantly higher current density compared with the pure CNF cathode at the same scan rate. With the increase of the scan rate, potential shifting of the cathodic and anodic peaks are significantly smaller in the presence of TaPcCo-MWCNT, which indicates effectively reduced cathode polarization, promoted polysulfide conversion kinetics, and accelerated Li-ion diffusion in the cathode.[42]

Li_2S nucleation and precipitation are typically regarded as the rate-determining processes during cell discharge. This is evidenced by the greater potential shifting of cathodic peak II at increasing CV scan rates for the pure CNF cell. Electrochemical Li_2S precipitation experiments further proof that TaPcCo-MWCNT facilitates the solid-liquid conversion of LiPSs to Li_2S. Cells containing a lithium foil anode, 0.2 M Li_2S_8 catholyte and a CNF based cathode with or without TaPcCo-MWCNT were examined. Cells were first stabilized at 2.08V and then kept at the constant voltage of 2.07V (a 0.01V overpotential to overcome the energy barrier) to measure the Li_2S precipitation current. As shown in Figure 4e-f, the measured current can be divided into contributions from the reduction of Li_2S_8, the reduction of Li_2S_6 and the precipitation of Li_2S.[22] The cell with TaPcCo-MWCNT (Figure 4f) exhibits an intense Li_2S precipitation current peak that occurs well ahead that of the pure CNF cell (Figure 4e), achieving an integrated sulfur specific capacity of 258.77 mAh g^{-1} which is nearly doubled that of the pure CNF cathode. The smooth transition of liquid-phase Li_2S_4 to solid-phase Li_2S_2 is also clearly evidenced from the significantly reduced voltage drop onset to the second discharge plateau (the phase transition overpotential[43]) as demonstrated in Figure S7 (SI).

The interaction between TaPcCo-MWCNT and LiPSs was further studied to reveal the catalytic mechanism of TaPcCo-MWCNT. Li_2S_6 adsorption test demonstrates the much stronger LiPSs adsorption capability of TaPcCo-MWCNT over CNF. The near-complete Li_2S_6 uptake by TaPcCo-MWCNT after 2 hours of immersion is further evidenced by the disappearance of the ultraviolet−visible absorbance peak at 432 nm (Figure S8, SI).

DFT calculations were carried out to investigate the LiPSs binding geometry (Li_2S_6 as a prototype) and the corresponding binding energy on TaPcCo-MWCNT. Energy minimization was performed and two adsorption geometries were obtained. The first (Figure 4h) takes place around the central Co atom, where the sulfiphilic Co atom bond with a terminal S atom of Li_2S_6 to form a Co-S bond of 2.469 Å whilst a nearest lithiophilic N atom on the Pc ring forms a N-Li bond of 2.290 Å. The corresponding binding energy was calculated to be -1.44 eV, which is significantly lower than that of a graphitic basal plane (c.a. -0.5 eV).[14] The strong LiPSs affinity arises from dual Lewis acid-base interactions, where Li atoms of LiPSs and Co atoms of TaPcCo are Lewis acidic sites, whilst the polysulfide moieties and the electron-negative N atoms in the Pc ring act as Lewis basic sites.[44] Catalysed LiPSs conversion is fundamentally enabled by the close binding geometry at a short bond length between the central Co atom of TaPcCo and a terminal S atom of the LiPSs. The half-filled d_z^2 orbital of the central Co atom in TaPcCo exhibits ultra-high electron transmission coefficient that enables electron superexchange [26] between the conductive MWCNT core and LiPSs, serving as an ‘electron highway’ to support continuous sulfur redox at elevated reaction kinetics.

The other potential LiPSs binding site (Figure 4i) is found at the peripheral amino substituent group with a moderate binding energy of -0.77 eV. The interaction involves the formation of a sole

Li-N bond with a short bond length of 2.085Å that can be attributed to the Li coordination with the electron lone-pairs in the amino nitrogen atoms. This further improves the Li-ion affinity of MWCNT-TaPcCo and facilitates Li-ion diffusion to and from the afore-mentioned sulfur redox catalytic sites around the central Co atoms.[45] The Li-ion diffusion coefficient D_{Li^+} was calculated form the CV peak I, II and III at different scan rates (Figure 4c-d) using the classic Randles−Sevcik equation. As shown in Figure S9 (SI), the slopes from all three CV peaks of TaPcCo-MWCNT/CNF are much higher than those of CNF. D_{Li^+} is calculated to be 3-10 times that of pure CNF (Table S1, SI), illustrating the significantly improved Li-ion diffusion rate and promoted polysulfide conversion kinetics in both the cathodic and anodic processes.

The interactions between the adsorbed Li_2S_6 and the TaPcCo-MWCNT adsorbent were also confirmed by XPS. The solids after the Li_2S_6 adsorption test were separated and dried in an Ar-filled glovebox before being subjected to the XPS measurements. The S2p spectrum (Figure 4j) presents a strong peak at 163.45 eV that can be attributed to the formed S-Co bonds with TaPcCo-MWCNT.[46] Peaks associated with the terminal (S_T^{-1}) and bridging (S_B) S atoms on the polysulfide chain were also resolved whilst the presence of the polythionate and thiosulfate features can be attributed to the inevitable contact with air during sample handling. A Li-N peak at 57.37 eV is also observed on the Li1s spectrum (Figure 5k), accompanying the main Li-S peak at 55.53 eV.[47] Comparisons of the Co2p (Figure 5l) and N1s (Figure 5m) spectra with the counterparts of bare TaPcCo-MWCNT suggest the formation of a new Co-S peak (778.14 eV)[46] and N-Li peak (402.38 eV)[22] respectively, which once again confirms the interactions of the sulfiphilic and lithiophilic binding sites on TaPcCo-MWCNT with the adsorbed Li_2S_6 molecules.

Li-S full cells were prepared and subjected to galvanostatic charge/discharge tests. The sulfur content in TaPcCo-MWCNT/CNF/S was confirmed by TGA under N_2 atmosphere to be 75 wt% (Figure S10, SI), leading to 60 wt% of sulfur in the cathode coatings. Cathodes with 2, 5 and 7 mg cm^{-2} areal sulfur loadings were considered and the effect of added TaPcCo-MWCNT in the cathode was compared. Specific capacities at elevating C rates were first evaluated for 2 mg cm^{-2} and 5 mg cm^{-2} areal sulfur loadings respectively, the capacities of the 5^{th} cycle at each C rate are quoted for comparisons. As seen in **Figure 5**a for the 2 mg cm^{-2} sulfur loading cell, a high discharge capacity of 1398 mAh g^{-1} at 0.2C was achieved with TaPcCo-MWCNT, which remained functioning well with the increase of the C rate and delivered specific capacities of 1197 mAh g^{-1}, 1010 mAh g^{-1}, 702 mAh g^{-1} and 614 mAh g^{-1} at 0.5C, 1C, 2C and 4C respectively.

The 5 mg cm^{-2} areal sulfur loading cells were first tested at electrolyte/sulfur (E/S) ratios of 4, 6 and 8 μL mg^{-1} to determine the optimized electrolyte amount for thick cathodes (Figure 5b and Figure S11 in SI). The best is found with the E/S ratio of 6 μL mg^{-1} and a higher or lower E/S ratio leads to reduced capacity retention over the tests or lower specific capacities above 1C, respectively. As shown in Figure 5b, TaPcCo-MWCNT shows a relatively small decrease in specific capacities compared with the 2 mg cm^{-2} counterpart at 0.2C, 0.5C and 1C. Even at the high rate of 2C, it still delivered a high specific capacity close to 600 mAh g^{-1}. In vast comparison, the cathode containing solely CNF exhibits significantly reduced specific capacities especially at high C rates and at 5 mg cm^{-2} high areal sulfur loading. Galvanostatic charge/discharge profiles at different C rates from cells with and without TaPcCo-MWCNT are plotted and compared in Figure 5c and Figure S12 (SI) for the 2 mg cm^{-2} and 5 mg cm^{-2} cells respectively. Voltage plateaus from cells with TaPcCo-MWCNT are well retained at increasing C rates, with smaller potential

polarizations in agreement with the CV results (Figure 4b). The second-discharge plateau is well-resolved with TaPcCo-MWCNT at the high rate of 4C, indicating the significantly reduced overpotentials from promoted LiPSs redox kinetics. At the further increased areal sulfur loading of 7 mg cm^{-2} (Figure S13, SI), a high specific capacity of 1025 mAh g^{-1} was obtained at 0.2C and close to 600 mAh g^{-1} was reserved at the high current density of 1 C. This clearly demonstrates the high sulfur utilzation with TaPcCo-MWCNT at elevated sulfur loadings.

Long-term cycling stability tests of the prepared cells were performed at 0.5C and the results are shown in Figure 5d. The cathode with TaPcCo-MWCNT at 2 mg cm^{-2} areal sulfur loading delivered an specific capacity of 1197 mAh g^{-1} in the first cycle. After 200 cycles, a high specific capacity of 1111 mAh g^{-1} was retained (92.8% capacity retention), corresponding to only 0.035% of capacity decay per cycle. Stable long-term cycling with high specific capacities were also observed on the 5 mg cm^{-2} sulfur loading cell **(**Figure 5d). At the higher sulfur loading, the initial specific capacity decreased marginally to 1075 mAh g^{-1} and the cell exhibited similar cycling stability, with 88.79% of capacity retained (950 mAh g^{-1}) after 200 cycles. The corresponding charge/discharge profiles from various cycles are shown in Figure 5e, cell polarization with the addition of TaPcCo-MWCNT is apparently mitigated.

Cycling stability at 1C high rate was further assessed on the 5 mg cm^{-2} areal sulfur loading cells and the results of three parallel cells TaPcCo-MWCNT are plotted in Figure 5f in areal capacity. The cells demonstrate a good repeatability at 1C. A high average initial areal capacity of 4.4 mAh cm^{-2} was achieved at 1C, of which 3.5 mAh cm^{-2} in average (79.5%) was retained after 500 cycles (0.0412 % of capacity decay per cycle). Charge/discharge profiles with increasing cycles numbers (Figure S14, SI) suggest that the two-plateau profiles were well retained and the increase in

electrode polarization was relatively small. The Coulombic efficiencies of cells containing TaPcCo-MWCNT stayed above 97% for all long-term cycling tests, illustrating good structural stability of both the cathodes and the anodes. In comparison, the CNF cathode without TaPcCo-MWCNT exhibited inferior initial specific capacities and low cycling stability. At elevated sulfur loading in particular (5mg cm^{-2} at 0.5C, Figure 5d), the cell delivered a low initial specific capacity of 607 mAh g^{-1} and encountered large fluctuation in Columbic efficiencies and rapid capacity decay over the 200 cycles of test.

Self-discharge with and without TaPcCo-MWCNT at 5mg cm^{-2} sulfur loading were examined after 200 charge/discharge cycles at 0.5C. Cells were fully charged to 2.9 V and their open circuit voltages (OCVs) were monitored for 24 hours (Figure S15, SI). The OCV of the pure CNF cell rapidly decreased to 2.25V whilst that with TaPcCo-MWCNT in the cathode remained above 2.38V. This can be attributed to the more completed conversion of LiPSs to sulfur during the charging process as well as strong LiPSs capturing with TaPcCo-MWCNT to mitigate the shuttle effect. Cells were also disassembled after the 200 charge/discharge cycles at 0.5C to evaluate the surface morphologies of cycled Li anodes. As shown in Figure S16 (SI), severe corrosions and structural fragmentations can be seen on the Li anode cycled with CNF/S whilst these are significantly reduced on the Li anode cycled with the TaPcCo-MWCNT/CNF/S cathode. This results from the effective suppression of LiPSs migration to the anode side with TaPcCo-MWCNT/CNF/S, which helps to protect the Li anode from the subsequent corrosions by the LiPSs and enables an extended cycle life of the Li anode.

Electrochemical impedance spectroscopy (EIS) results further reveal the improved sulfur management with TaPcCo-MWCNT along cell cycling. Nyquist plots from 5mg cm^{-2} fresh cells

with and without TaPcCo-MWCNT (Figure S17, SI) both consist of one depressed semicircle at the high frequency range correlating to the cathode/electrolyte charge transfer impedance (R_{ct}), as well as an inclined tail in the low frequency region associated with Li-ion diffusion (W_0).[48] The intercept at high frequencies originates from the resistance of essential cell components such as the current collectors (R_0). Equivalent circuits that were used to analyse the obtained Nyquist plots are presented in Figure S18 (SI) and the fitted parameters are shown in Table S2 (SI). The reduced R_{ct} in the presence of TaPcCo-MWCNT is consistence with the improved sulfur utilization and redox kinetics. Nyquist plots after 200 cycles of charge/discharge tests at 0.5C are also plotted in Figure 5g. An additional semicircle at the middle range of frequency is observed on the pure CNF cell that may be attributed to the impedance of a Li_2S layer (R_s) formed on the cathode surface resulted from LiPSs dissolution and shuttling.[10a, 48] The absence of this additional semicircle with TaPcCo-MWCNT can be attributed to the highly localized sulfur utilization enabled by the effective LiPSs adsorption and their subsequent rapid conversion to the solid phase. Calculated R_{ct} from the cell with TaPcCo-MWCNT remained significantly lower after 200 cycles at 0.5C, demonstrating its structural integrity and stable redox promotion with cell cycling.

The cells were disassembled after 200 cycles at 0.5C in the discharged state to verify their differences in cathode surface morphologies. At low magnifications, the cathode containing TaPcCo-MWCNT exhibits a smooth and uniform surface (Figure 5h and Figure S19 in SI) whist irregular protrusions and cracks are observed on the pure CNF cathode (Figure 5i and Figure S20 in SI), indicating nonuniform volume expansions of the discharge-formed Li_2S. At elevated magnifications, the deposited Li_2S on the cathode containing TaPcCo-MWCNT (Figure 5j and Figure S19 in SI) are found to exist as thin films uniformly embedded in the network of TaPcCo-

MWCNTs and CNFs that are both clearly resolved (indicated in Figure 5j). On the pure CNF cathode (Figure 5k and Figure S20 in SI),on the other hand, the cathode surface is found to be covered by a layer of deposited Li_2S with greater thickness and no CNFs were observed on the cathode surface (The curved edges of the Li_2S films should be carefully distinguished from the straight and thicker CNFs seen in Figure 5j). The detachment of this insulating layer of Li_2S from the conductive CNFs means that they would not be re-utilized during the cell charging process.

The catalysed Li-S redox mechanism on TaPcCo-MWCNT was further studied using DFT calculations and the results are shown in **Figure 6**. To reduce computation expenses, models based on graphitic carbon slabs linked with TaPcCo *via* a C-NH-C secondary amine bridge at the same bond angles as the geometry optimized models in Figure 1 were employed to simulate TaPcCo-MWCNT (model denoted as TaPcCo-carbon in Figure 6) whilst pristine graphitic carbon slabs (model denoted as Carbon in Figure 6) were used to represent CNF. Li_2S deposition from liquid phase LiPSs is first found to be energetically more favourable on the model of TaPcCo-carbon. The Gibbs free energies associated with the stepwise reduction of S_8 to Li_2S through a sequence of reference LiPSs were first calculated,[49] and the obtained energy profiles are presented in Figure 6a with corresponding adsorption geometries of sufur-containing species shown inset. On the pristine graphitic surface, S_8 undergoes continuous exothermic conversions to Li_2S_2, followed by a high endothermic energy jump from Li_2S_2 to Li_2S. This large positive free energy indicates the high energy barrier of Li_2S formation as the reaction bottle-neck in the whole discharge redox process. On the TaPcCo-carbon model, this process is significantly ameliorated by the gradual endothermic conversions from Li_2S_8 to Li_2S through all LiPSs intermediates. As a result, the Gibbs free energy for the conversion of Li_2S_2 to Li_2S with TaPcCo-carbon is greatly reduced from 1.55

eV to 0.18 eV. Compared with the pure CNF cathode, the significantly improved capacity retention and sulfur utilization with TaPcCo-MWCNT can be largely attributed to the reduced energetic irreversibility of the liquid-solid transitions between soluble LiPSs and Li_2S. On the kinetics side, the promoted Li_2S precipitation redox during cell discharge at the presence of TaPcCo-MWCNT has already been demonstrated by direct electrochemical measurements (Figure 4e-f).

The reverse kinetics of Li_2S decomposition ($Li_2S \rightarrow LiS + Li^+ + e^-$) was further explored theoretically using the climbing image nudged elastic band method to calculate the delithiation energy barrier of Li-S bond breaking. The obtained energy profiles presented in Figure 6b clearly reveal the greatly reduced Li_2S decomposition energy barrier on the TaPcCo-carbon model (0.98 eV) in comparison with a pristine graphitic surface (2.2 eV). This is consistent with the reduced overpotential onset to the first charge plateau as shown in Figure S21 (SI). Figure 6c-d shows the corresponding Li-ion migration pathways during Li_2S dissociation. The initial, transition and final states of Li_2S decomposition on the TaPcCo-carbon and pristine graphitic models are shown in Figure S22 (SI) and Figure S23 (SI) respectively. Compared with the pristine graphitic surface that presents a low Li-ion affinity (Figure 6d), the Li-ion migration pathway on the TaPcCo-carbon model (Figure 6c) is obviously associated with the highly lithiophilic N atoms on the Pc ring and the substituent amino group. Migration of the remaining LiS cluster towards the amino group at the other side of the Pc ring is also visible, which may be attributed to the strong N-Li interactions as well. This plays a key role in promoting the Li_2S decomposition kinetics towards improved sulfur utilization during the cell charging process.

3. Conclusion

MWCNTs covalently modified by TaPcCo were synthesized and used as a highly effective Li-S redox catalysis material for Li-S batteries. LiPSs binding is facilitated by the sulfiphilic central Co atom and the lithiophilic N atoms on the Pc ring of TaPcCo. The MWCNT core that is covalently bonded with the TaPcCo molecules enables fast electron transport to and from the active catalytic sites of the central Co atom, of which the unoccupied d-orbital acts as an electron highway that greatly promotes the cathode sulfur redox in the liquid phase and during liquid-solid transitions of Li_2S deposition and decomposition. The substituent amino groups of TaPcCo with high Li-ion affinity provide fast Li-ion transport whist contribute to the reduction of Li_2S decomposition energy barrier. Significantly improved sulfur utilization and capacity retention were obtained at the presence of TaPcCo-MWCNT under high areal sulfur loadings and C rates simultaneously, demonstrating its potential for future scale-ups.

Supporting Information

Supporting Information is available from the Wiley Online Library or from the author.

Acknowledgements

C.H. acknowledges the support from the Natural Science Foundation of Shandong Province (Grant No. ZR2019QEM001) and the Fundamental Research Funds of Shandong University (Grant No. 2018JC038). Z.Q. thanks the support from the Young Scholars Program of Shandong University.

Received: ((will be filled in by the editorial staff))
Revised: ((will be filled in by the editorial staff))
Published online: ((will be filled in by the editorial staff))

References

[1] L. F. Nazar, M. Cuisinier, Q. Pang, MRS Bull. **2014**, *39*, 436.

[2] Y. Yang, G. Lu, Y. Li, Z. Liu, X. Huang, ACS Appl. Mater. Interfaces **2013**, *5*, 13478.

[3] M. A. Pope, I. A. Aksay, Adv. Energy Mater. **2015**, *5*, 1500124.

[4] A. Eftekhari, D.-W. Kim, J. Mater. Chem. A. **2017**, *5*, 17734.

[5] a) D. Liu, C. Zhang, G. Zhou, W. Lv, G. Ling, L. Zhi, Q.-H. Yang, Adv. Sci. **2018**, *5,*1700270; b) M. Wild, L. O'Neill, T. Zhang, R. Purkayastha, G. Minton, M. Marinescu, G. J. Offer, Energy Environ. Sci. **2015**, *8*, 3477.

[6] H. Yamin, A. Gorenshtein, J. Penciner, Y. Sternberg, E. Peled, J. Electrochem. Soc. **1988**, *135*, 1045.

[7] M. Hagen, D. Hanselmann, K. Ahlbrecht, R. Maça, D. Gerber, J. Tübke, Adv. Energy Mater. **2015**, *5*, 1401986.

[8] Z.-W. Zhang, H.-J. Peng, M. Zhao, J.-Q. Huang, Adv. Funct. Mater. **2018**, *28*, 1707536.

[9] a) Y. Z. Song, W. Zhao, X. Y. Zhu, L. Zhang, Q. C. Li, F. Ding, Z. F. Liu, J. Y. Sun, ACS Appl. Mater. Interfaces **2018**, *10*, 15733; b) H. Lin, S. Zhang, T. Zhang, H. Ye, Q. Yao, G. W. Zheng, J. Y. Lee, Adv. Energy Mater. **2018**, *8,* 1801868.

[10] a) H. Wu, Y. Li, J. Ren, D. Rao, Q. Zheng, L. Zhou, D. Lin, Nano Energy **2019**, *55*, 82; b) L. Zhang, Z. Chen, N. Dongfang, M. Li, C. Diao, Q. Wu, X. Chi, P. Jiang, Z. Zhao, L. Dong, R. Che, K. P. Loh, H. Lu, Adv. Energy Mater. **2018**, *8*, 1870152.

[11] a) T. Li, C. He, W. Zhang, J. Mater. Chem. A. **2019**, *7*, 4134; b) Z. Li, Q. He, X. Xu, Y. Zhao, X. Liu, C. Zhou, D. Ai, L. Xia, L. Mai, Adv. Mater. **2018**, *30*, 1804089.

[12] a) N. Wang, B. Chen, K. Qin, E. Liu, C. Shi, C. He, N. Zhao, Nano Energy **2019**, *60*, 332; b) J. He, G. Hartmann, M. Lee, G. S. Hwang, Y. Chen, A. Manthiram, Energy Environ. Sci. **2019**, *12*, 344.

[13] a) Y. Luo, N. Luo, W. Kong, H. Wu, K. Wang, S. Fan, W. Duan, J. Wang, Small **2018**, *14*, 1702853; b) Y. Zhong, L. Yin, P. He, W. Liu, Z. Wu, H. Wang, J. Am. Chem. Soc. **2018**, *140*, 1455.

[14] S. Shen, X. Xia, Y. Zhong, S. Deng, D. Xie, B. Liu, Y. Zhang, G. Pan, X. Wang, J. Tu, Adv. Mater. **2019**, *31,* 1900009.

[15] a) A. Indra, T. Song, U. Paik, Adv. Mater. **2018**, *30,* 1705146; b) J. Zhou, R. Li, X. Fan, Y. Chen, R. Han, W. Li, J. Zheng, B. Wang, X. Li, Energy Environ. Sci. **2014**, *7*, 2715.

[16] a) J. He, A. Manthiram, Energy Storage Mater. **2019**, *20*, 55; b) W.-G. Lim, S. Kim, C. Jo, J. Lee, Angewandte Chemie International Edition **2019**, *58*, 18746.

[17] G. Babu, N. Masurkar, H. Al Salem, L. M. R. Arave, J. Am. Chem. Soc. **2017**, *139*, 171.

[18] X. Tao, J. Wang, C. Liu, H. Wang, H. Yao, G. Zheng, Z. W. Seh, Q. Cai, W. Li, G. Zhou, C. Zu, Y. Cui, Nat. Commun. **2016**, *7*, 11203.

[19] a) H. J. Peng, G. Zhang, X. Chen, Z. W. Zhang, W. T. Xu, J. Q. Huang, Q. Zhang, Angew. Chem. Int. Ed. **2016**, *55*, 12990; b) F. Zhou, Z. Li, X. Luo, T. Wu, B. Jiang, L.-L. Lu, H.-B. Yao, M. Antonietti, S.-H. Yu, Nano Lett. **2018**, *18*, 1035.

[20] a) C. Ye, Y. Jiao, H. Y. Jin, A. D. Slattery, K. Davey, H. H. Wang, S. Z. Qiao, Angew. Chem. Int. Ed. **2018**, *57*, 16703; b) L. Zhang, X. Chen, F. Wan, Z. Niu, Y. Wang, Q. Zhang, J. Chen, ACS Nano **2018**, *12*, 9578.

[21] a) Y. Mi, W. Liu, X. Li, J. Zhuang, H. Zhou, H. Wang, Nano. Res. **2017**, *10*, 3698; b) J. Shen, X. Xu, J. Liu, Z. Liu, F. Li, R. Hu, J. Liu, X. Hou, Y. Feng, Y. Yu, M. Zhu, ACS Nano **2019**, *13*, 8986

[22] T. Zhou, W. Lv, J. Li, G. Zhou, Y. Zhao, S. Fan, B. Liu, B. Li, F. Kang, Q.-H. Yang, Energy Environ. Sci. **2017**, *10*, 1694.

[23] A. Hamwi, H. Alvergnat, S. Bonnamy, F. Béguin, Carbon **1997**, *35*, 723.

[24] A. B. Sorokin, Chem. Rev. **2013**, *113*, 8152.

[25] W. Huang, Z. Lin, H. Liu, R. Na, J. Tian, Z. Shan, J. Mater. Chem. A. **2018**, *6*, 17132.

[26] a) S. Fletcher, N. J. Van Dijk, The J. Phy. Chem. C **2016**, *120*, 26225; b) B. Q. Li, H. J. Peng, X. Chen, S. Y. Zhang, J. Xie, C. X. Zhao, Q. Zhang. CCS Chem **2019**, *1*, 128; b) H. Liao, H. Wang, H. Ding, X. Meng, H. Xu, B. Wang, X. Ai, C. Wang. J. Mater. Chem. A. **2016**, *4*, 7416.

[27] W. Zeng, L. Wang, X. Peng, T. Liu, Y. Jiang, F. Qin, L. Hu, P. K. Chu, K. Huo, Y. Zhou, Adv. Energy Mater. **2018**, *8*, 1702314.

[28] B. N. Achar, P. K. Jayasree, Synth. Met. **1999**, *104*, 101.

[29] R. L. Zhang, R. Q. Wang, K. Luo, W. P. Zhang, J. S. Zhao, S. C. Zhang, J. Electrochem. Soc. **2014**, *161*, H941.

[30] W. X. Yang, R. L. Zhang, K. Luo, W. P. Zhang, J. S. Zhao, Rsc Adv. **2016**, *6*, 75632.

[31] E. D. Bergmann, E. Zimkin, S. Pinchas, J. Royal Nether. Chem. Soc. **1952**, *71*, 168.

[32] Y. Hu, W. Chen, T. Lei, B. Zhou, Y. Jiao, Y. Yan, X. Du, J. Huang, C. Wu, X. Wang, Y. Wang, B. Chen, J. Xu, C. Wang, J. Xiong, Adv. Energy Mater. **2019**, *9,* 1802955.

[33] B. Farbos, T. Tassaing, Phys. Chem. Chem. Phys. **2009**, *11*, 5052.

[34] a) Y. Y. Li, X. Z. Wu, C. Liu, S. Wang, P. F. Zhou, T. Zhou, Z. C. Miao, W. Xing, S. P. Zhuo,

J. Zhou, J. Mater. Chem. A. **2019**, *7*, 7128; b) Y. Li, Y. Feng, W. Feng, Electrochim. Acta **2013**, *107*, 343.

[35] K. N. Mehrotra, B. P. Giri, Synthesis **1977**, *1977*, 489.

[36] T. Palacin, H. Le Khanh, B. Jousselme, P. Jegou, A. Filoramo, C. Ehli, D. M. Guldi, S. Campidelli, J. Am. Chem. Soc. **2009**, *131*, 15394.

[37] Z.-H. Sheng, L. Shao, J.-J. Chen, W.-J. Bao, F.-B. Wang, X.-H. Xia, ACS Nano **2011**, *5*, 4350.

[38] Z. Khan, S. O. Park, J. Yang, S. Park, R. Shanker, H.-K. Song, Y. Kim, S. K. Kwak, H. Ko, J. Mater. Chem. A. **2018**, *6*, 24459.

[39] a) R. Burkitt, T. R. Whiffen, E. H. Yu. Appl Catal B **2016**, *181*, 279; b) E. P. Nguyen, B. J. Carey, C. J. Harrison, P. Atkin, K. J. Berean, E. Della Gaspera, J. Z. Ou, R. B. Kaner, K. Kalantar-Zadeh, T. Daeneke. Nanoscale **2016**, *8*, 16276.

[40] J. Wang, G. Yang, J. Chen, Y. Liu, Y. Wang, C. Y. Lao, K. Xi, D. Yang, C. J. Harris, W. Yan, S. Ding, R. V. Kumar, Adv. Energy Mater. **2019**, *9,* 1902001.

[41] C. Hu, S. Sedghi, A. Silvestre-Albero, G. G. Andersson, A. Sharma, P. Pendleton, F. Rodríguez-Reinoso, K. Kaneko, M. J. Biggs, Carbon **2015**, *85*, 147.

[42] Y. Tao, Y. Wei, Y. Liu, J. Wang, W. Qiao, L. Ling, D. Long, Energy Environ. Sci. **2016**, *9*, 3230.

[43] F. Y. Fan, W. C. Carter, Y.-M. Chiang, Adv. Mater. **2015**, *27*, 5203.

[44] J. C. Ye, J. J. Chen, R. M. Yuan, D. R. Deng, M. S. Zheng, L. Cronin, Q. F. Dong, J. Am. Chem. Soc. **2018**, *140*, 3134.

[45] F.-S. Li, Y.-S. Wu, J. Chou, M. Winter, N.-L. Wu, Adv. Mater. **2015**, *27*, 130.

[46] Z.-Y. Wang, L. Wang, S. Liu, G.-R. Li, X.-P. Gao, Adv. Funct. Mater. **2019**, *29*,1901051.

[47] D. Su, M. Cortie, G. Wang, Adv. Energy Mater. **2017**, *7*,1602014.

[48] Q. Yu, Y. Lu, R. Luo, X. Liu, K. Huo, J.-K. Kim, J. He, Y. Luo, Adv. Funct. Mater. **2018**, *28*,1804520.

[49] a) Z. Du, X. Chen, W. Hu, C. Chuang, S. Xie, A. Hu, W. Yan, X. Kong, X. Wu, H. Ji, L.-J. Wan, J. Am. Chem. Soc. **2019**, *141*, 3977; b) L. Du, Q. Wu, L. Yang, X. Wang, R. Che, Z. Lyu, W. Chen, X. Wang, Z. Hu, Nano Energy **2019**, *57*, 34.

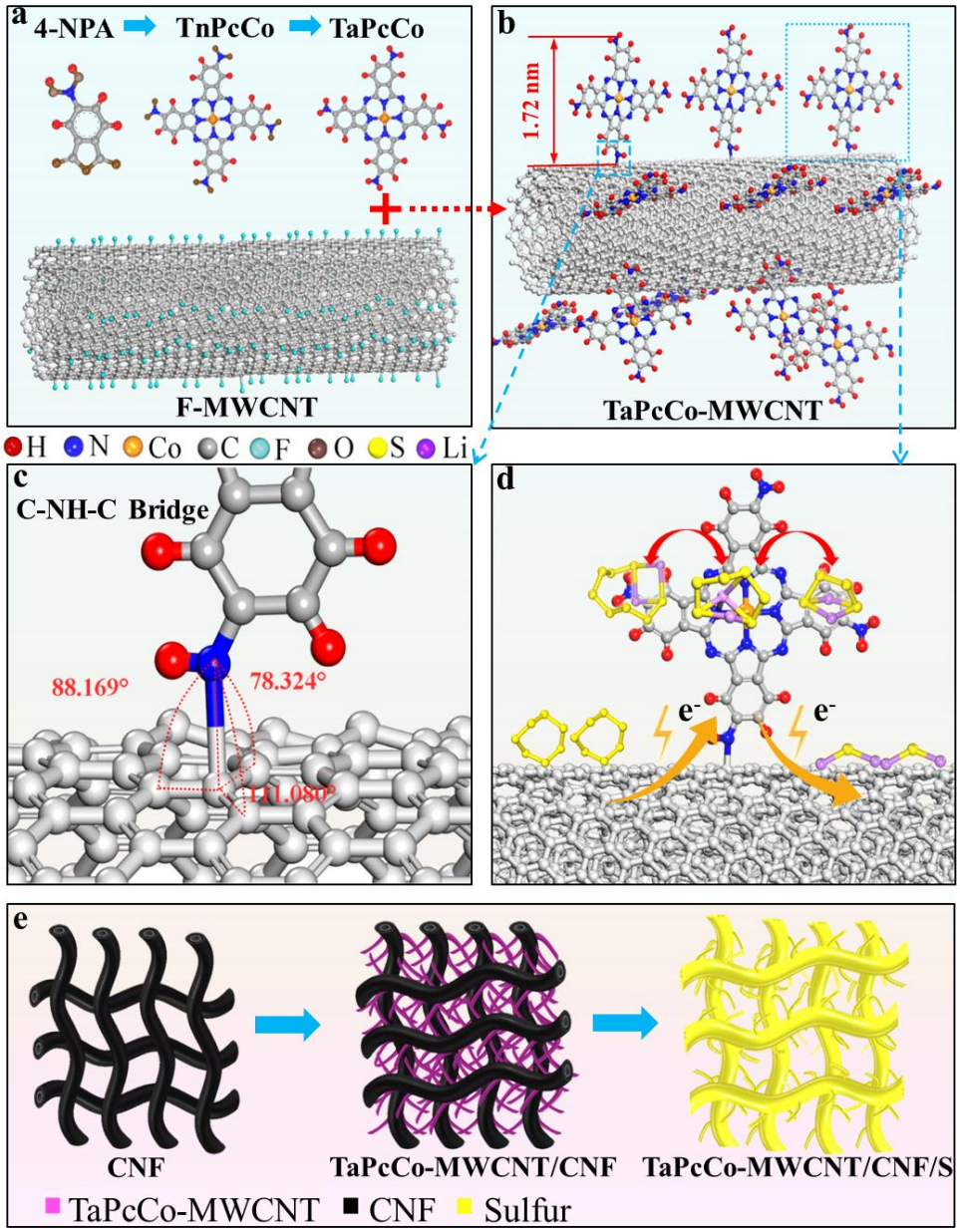

Figure 1. Schematic illustration of: a) 4-nitrophthalic anhydride, TnPcCo, TaPcCo and F-MWCNT structures; b) geometry optimized TaPcCo-MWCNT structure; c) geometry optimized -NH- covalent linkage between TaPcCo and MWCNT; d) LiPSs adsorption and catalysed sulfur redox on TaPcCo-MWCNT; d) preparation of the TaPcCo-MWCNT/CNF/S cathode composite.

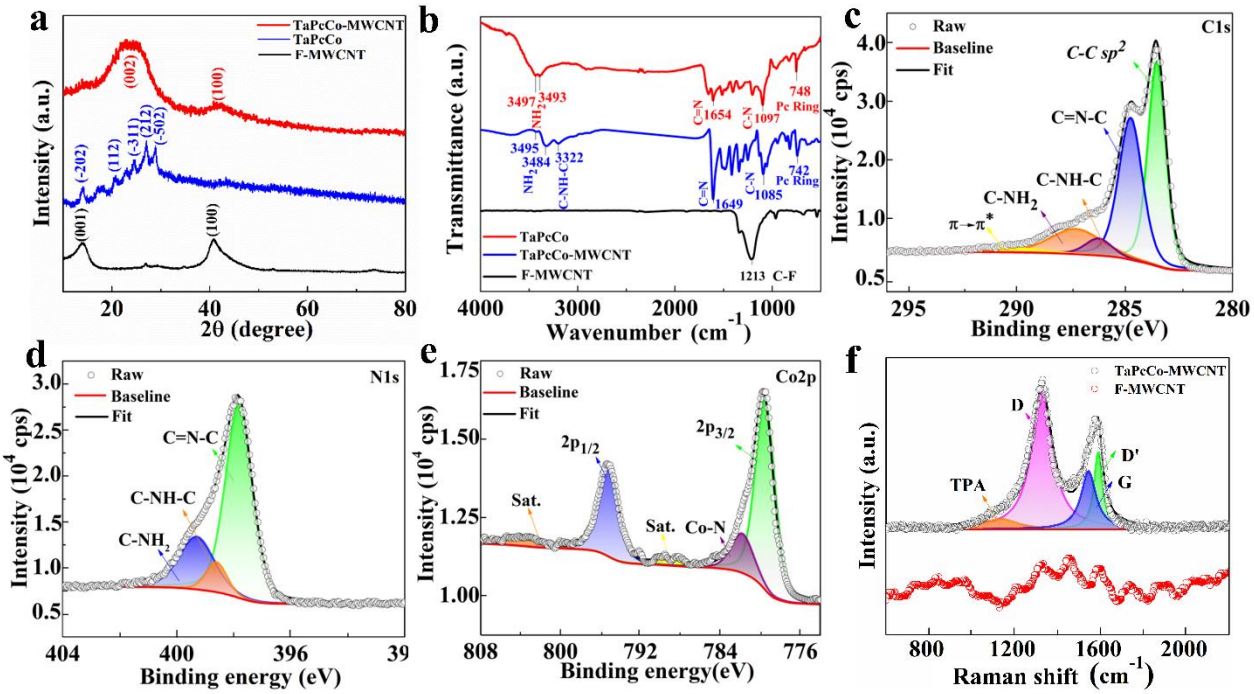

Figure 2. Stuctural and chemical characterization of TaPcCo-MWCNT. a) XRD patterns of TaPcCo, F-MWCNT and TaPcCo-MWCNT. b) FTIR spectra of TaPcCo, F-MWCNT and TaPcCo-MWCNT. c) XPS high-resolution C1s spectrum of TaPcCo-MWCNT. d) XPS high-resolution N1s spectrum of TaPcCo-MWCNT. e) XPS high-resolution Co2p spectra of TaPcCo-MWCNT. f) Raman spectra of TaPcCo-MWCNT and F-MWCNT.

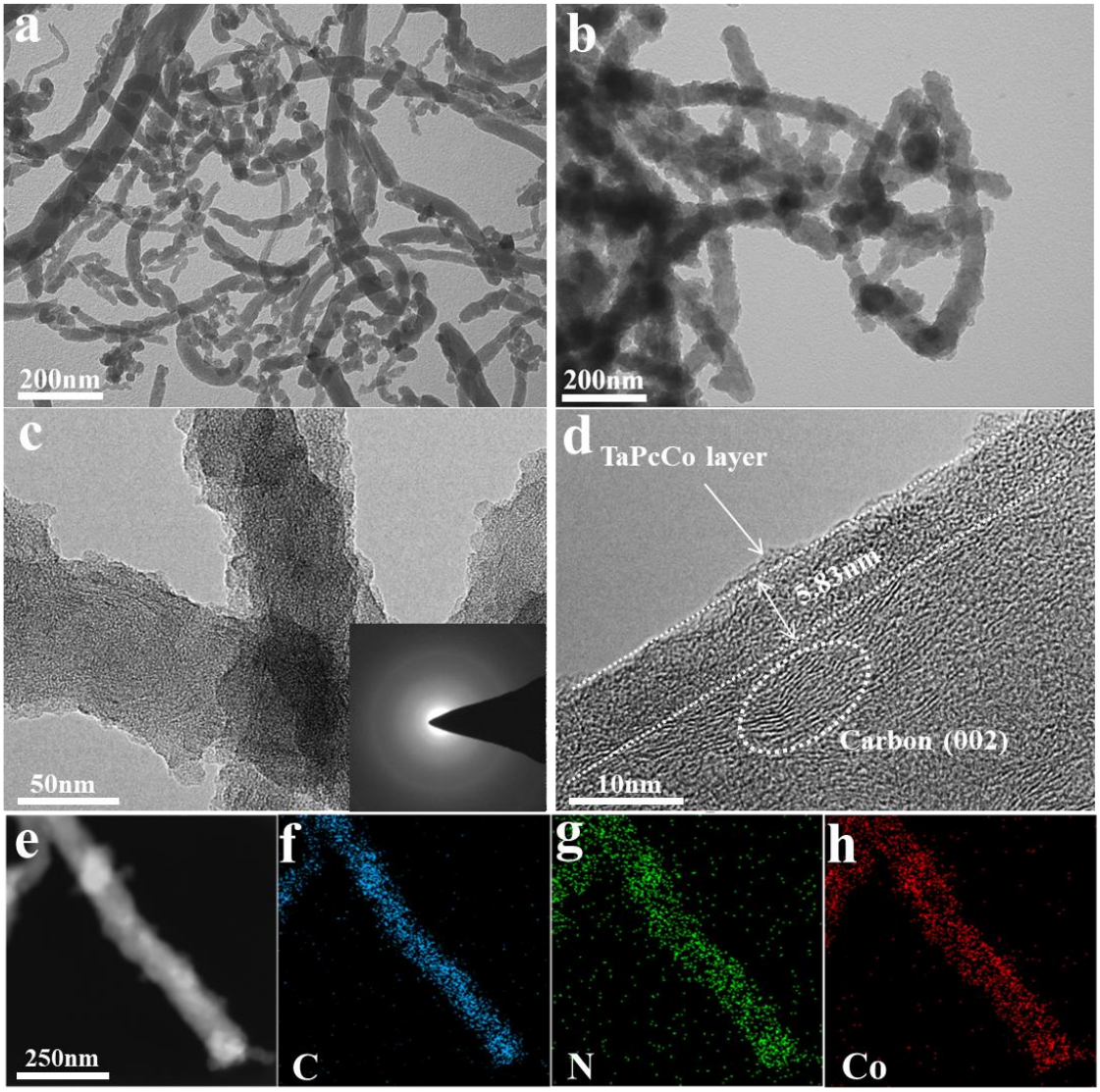

Figure 3. TEM microstructure of TaPcCo-MWCNT. a) low-magnification TEM image of F-MWCNT. b) low-magnification TEM image of TaPcCo-MWCNT. c-d) High-resolution TEM images of TaPcCo-MWCNT with the SAED pattern shown inset of c). e) HAADF image of TaPcCo-MWCNT and corresponding elemental distributions of f) element C, g) element N and h) element Co. (e) to (g) share the same scale bar in (e).

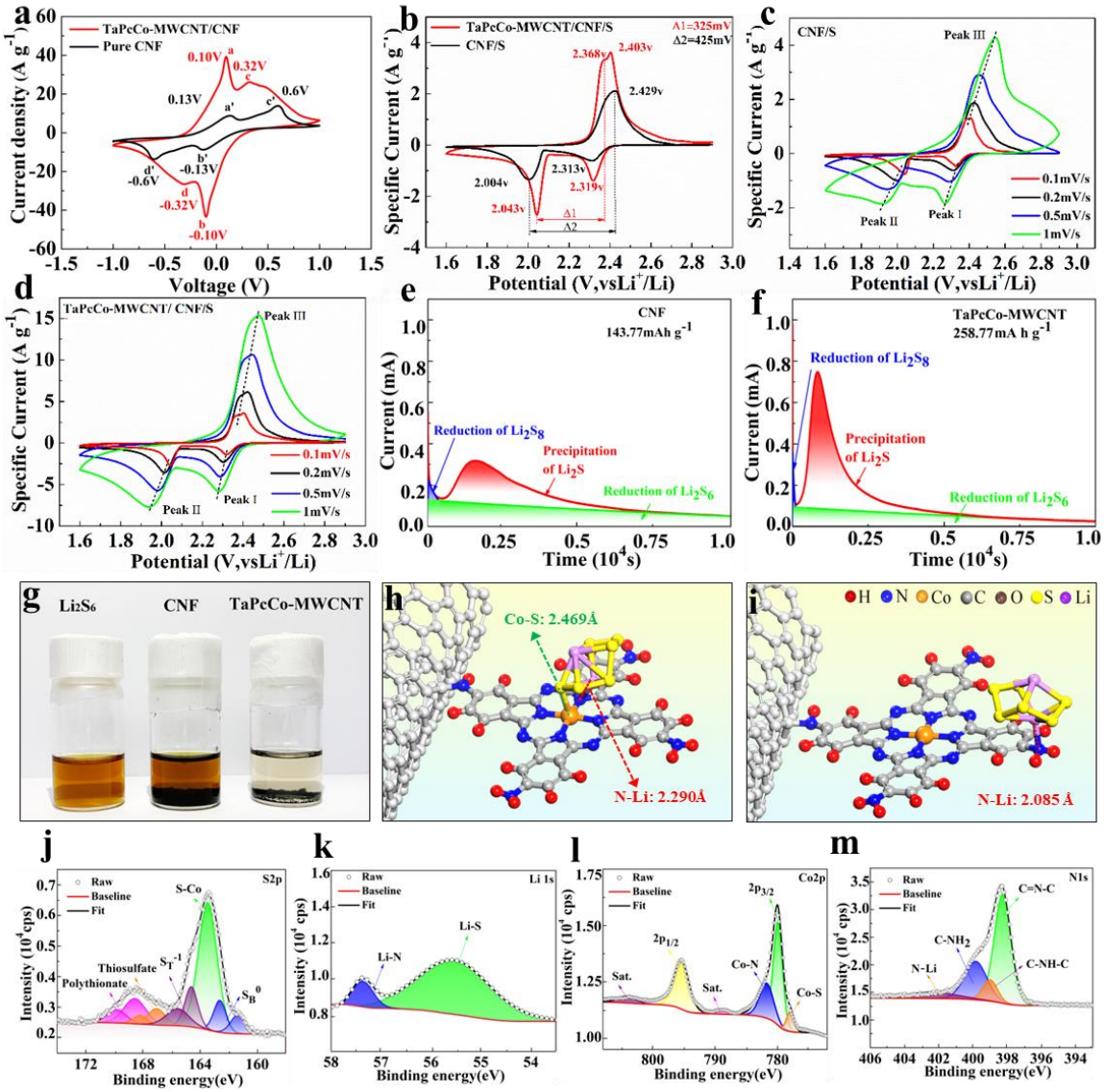

Figure 4. a) CV profiles of symmetric cells at 3 mV s^{-1}. b) CV profiles of Li-S full cells at 0.1 mV s^{-1}. c-d) CV profiles at elevating scan rates for Li-S full cells c) with TaPcCo-MWCNT and d) without TaPcCo-MWCNT. e-f) Li_2S nucleation and precipitation current profiles e) with TaPcCo-MWCNT and f) without TaPcCo-MWCNT. g) Comparison of solution phase Li_2S_6 uptake by CNF and TaPcCo-MWCNT. h-i) DFT calculated Li_2S_6 adsorption geometry on h) central Co atom and i) substituent amino group. j-m) XPS high-resolution spectra of TaPcCo-MWCNT with adsorbed Li_2S_6: j) S2p, k) Li1s, l) Co2p and m) N1s.

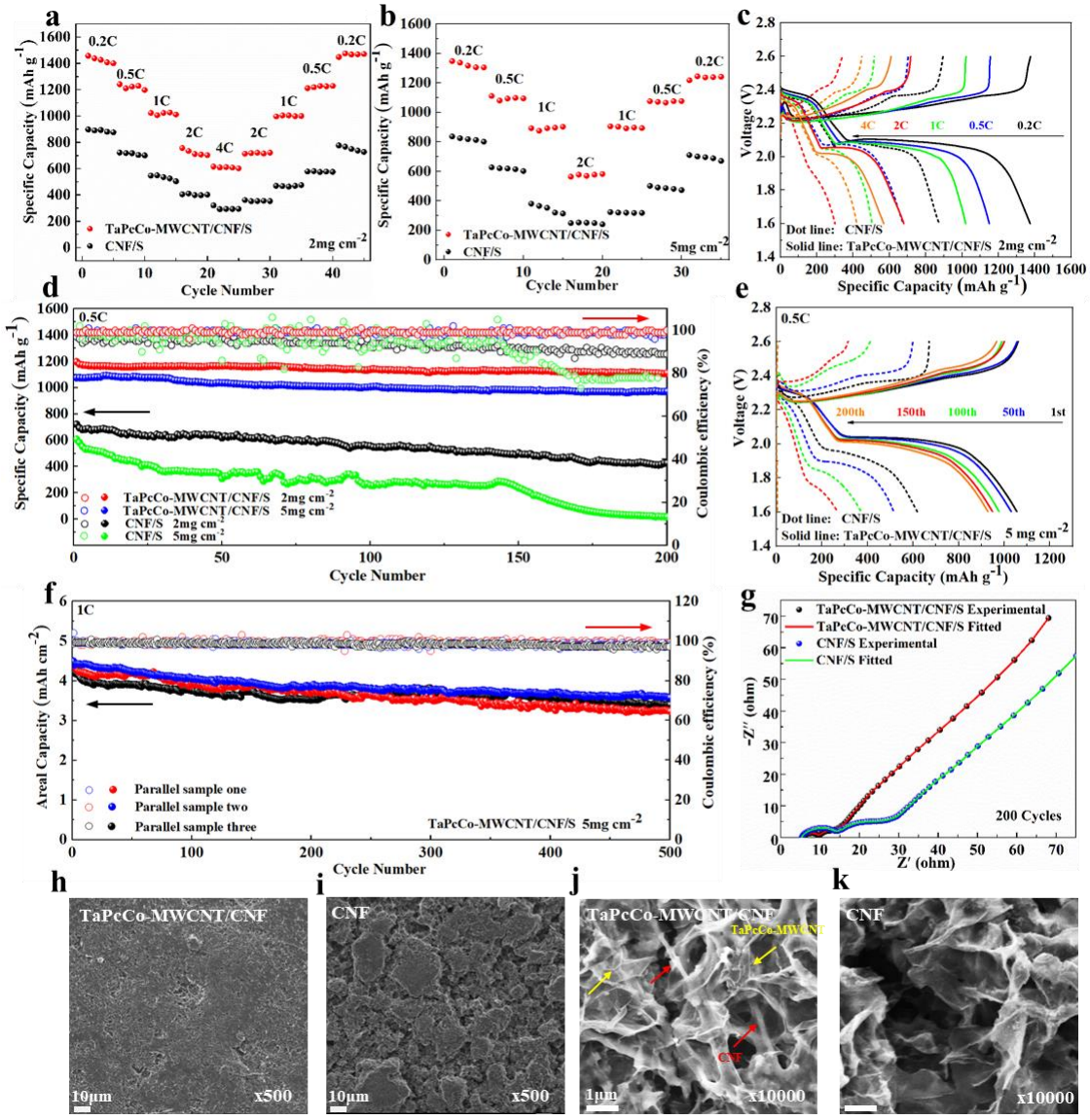

Figure 5. a-b) Cathode high-rate capability at various current densities at the areal sulfur loading of a) 2 mg cm^{-2} and b) 5 mg cm^{-2}. c) Galvanostatic charge/discharge profiles at various C rates under 2 mg cm^{-2} sulfur loading. d) Cycling performance 0.5C with 2 and 5 mg cm^{-2} areal sulfur loadings. e) Galvanostatic charge/discharge profiles from various cycles at 0.5C and 5 mg cm^{-2} areal sulfur loading. f) Charge/discharge cycling performance of TaPcCo-MWCNT/CNF/S at 1C with 5 mg cm^{-2} areal sulfur loading. g) EIS Nyquist plots of cells after 200 charge/discharge cycles at 0.5C. h-k) SEM morphologies of cathodes at h-i) low and g-k) high magnifications. h) and j) with TaPcCo-MWCNT, i) and k) without TaPcCo-MWCNT.

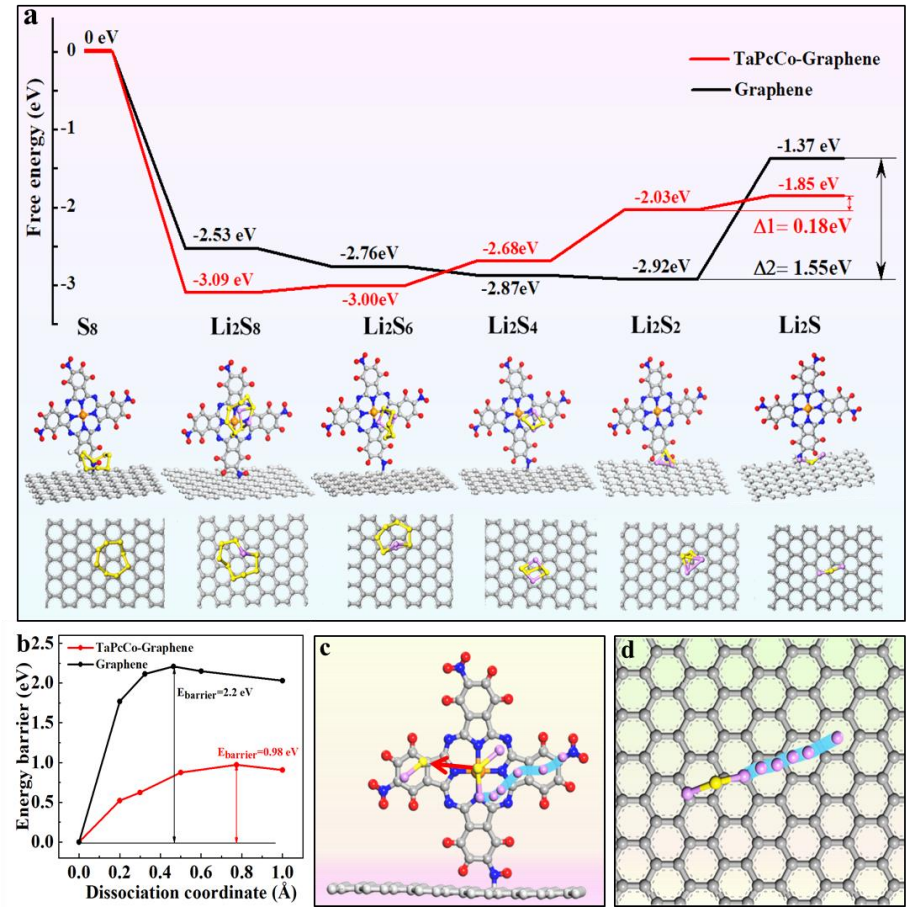

Figure 6. a) Free energy profiles for the reduction of S_8 to Li_2S *via* a range of reference LiPSs on TaPcCo-carbon and pristine graphitic models. Optimized adsorption geometries of sulfur-containing species are also provided. b) Energy profiles for the decomposition of Li_2S on TaPcCo-carbon and pristine graphitic models. c-d) The Li_2S decomposition pathway on c) TaPcCo-carbon and d) pristine graphitic surface. Grey, yellow, pink, blue and orange balls represent C, S, Li, N, and Co atoms, respectively.

Supporting Information

Multiwall Carbon Nanotubes Covalently Modified by Cobalt (II) Tetraaminophthalocyanines as an Efficient Sulfur Redox Catalyst for High-performance Lithium-Sulfur Batteries

*Xiao-Xia Yang, Wen-Zheng Du, Xu-Ting Li, Yang Zhang, Zhao Qian, Mark James Biggs, and Cheng Hu**

E-mail: c.hu@sdu.edu.cn

Experimental Section

Preparation of TnPcCo: 60 ml nitrobenzene containing 3.86 g 4-nitrophthalic anhydride, 0.05 g ammonium molybdate, 6.00 g urea and 1.20 g cobalt chloride hexahydrate were well mixed and refluxed at 185 °C under magnetic stirring for 4 hours. The product was separated by centrifugation and washed with toluene, mixed methanol and diethyl ether (1:9, v/v), mixed ethyl acetate and hexane (2:1, v/v) as well as ethanol.

Preparation of TaPcCo: 0.75 g of TnPcCO and 3 g of sodium sulfide nonahydrate were mixed in 30 ml of nitrogen-nitromethylamide and refluxed at 60 °C for 2 hours under magnetic stirring. The product was diluted in 150 ml of ice water, separated by centrifugation and washed with mixed methanol and diethyl ether (1:9, v/v) and methanol.

Preparation of TaPcCo-MWCNT: 0.1g fluorinated MWCNT (56.72 wt% F, JCNANO, China) and 0.2g TaPcCo were mixed and sonicated for 30 min in 50 ml of dimethyl sulfoxide to form a uniform suspension. 200 μl of pyridine was then added into the above suspension and the mixture was heated at 170 °C for 12 hours under magnetic stirring in N_2 atmosphere. The product was filterd and washed with dimethyl sulfoxide, N, N-dimethylformamide and methanol.

Preparation of TaPcCo-MWCNT/CNF/S: TaPcCo-MWCNT and CNF were mixed at the mass ratio of 3:7 and homogenized in water using a high-shear mixer to form a stable suspension. The suspension was filtered and the resulting TaPcCo-MWCNT/CNF was freeze-dried. To prepare the TaPcCo-MWCNT/CNF/S cathode composite, sulfur was finely ground with TaPcCo-MWCNT/CNF at the mass ratio of 75:25 and heated at 155 °C in Ar for 12 hours to enable uniform sulfur distribution. For comparison, the CNF/S cathode composite without TaPcCo-MWCNT was also prepared at the same sulfur loading of 75 wt%.

Materials characterization: XRD was performed on a BRUKER D8 Dmax-2500 diffractometer equipped with Cu Kα radiation. XPS was carried out using a KRATOS XSAM800 spectrometer with Al Kα radiation. IR spectra were collected on a BRUKER ALPHA spectrometer using KBr pellets. Elemental analysis was performed using a LECO TruSpec Micro CHN analyzer following the ASTM D 5373-02 standard. The instrument was calibrated using acetanilide. Raman spectroscopy was performed on a RENISHAW inVia confocal Raman microscope using a 532 nm laser beam. Reduced χ^2 values between around 1.5 were obtained for spectrum fitting (Values in the range of 1–3 indicate good fits).[1] Surface morphologies were observed on a field-emission-gun SEM (JEOL, JSM-7800F) operated at 3 kV. Microstructure analysis were performed on a field-emission-gun TEM (FEI, Tecnai G2 F20) operated at 200 kV. The corresponding elemental mappings were obtained using an OXFORD INSTRUMENTS, X-max 80T energy dispersive x-ray spectrometer. The sulfur loading content of the cathode composite was measured by TGA (NETZSCH, TG209) from room temperature to 800 °C at 5 °C min^{-1} under Ar atmosphere. Li_2S_6 adsorption tests were performed by immersing 10 mg adsorbents (CNF or TaPcCo-MWCNT) into 2 ml of 5 mM Li_2S_6 solution and soaked for 2 hours. A 0.5 M Li_2S_6 stock solution was prepared by

reacting sulfur and Li_2S at the molar ratio of 5:1 in a mixed DOL/DME solvent (1:1, v/v) at 65 °C for 24 hours under Ar protection. Li_2S_6 concentrations before and after the adsorption tests were measured using UV-Vis spectroscopy (PERKIN ELMER, Lambda 35) in the wavelength region of 300-800 nm.

Electrochemical measurements: For symmetric cells assembly, TaPcCo-MWCNT/CNF (or pristine CNF) and PVDF binder were mixed in N-methylpyrrolidone (NMP) at a mass ratio of 8:2 and ground to form a homogeneous slurry. The slurry was then coated onto Al foils, vacuum dried at 50 °C, and pouched into 12 mm diameter discs to use as both working and counter electrodes. The active material loading was controlled to be around 1mg cm^{-2}. CR2025 cases were used for cell assembly and each cell contained 30 µl of electrolyte composed of 0.2 M Li_2S_6 and 1 M lithium bis-trifluoromethanesulfonimide (LiTFSI) in mixed 1,2-dimethoxyethane (DME) and 1,3-dioxolane (DOL) (v/v, 1:1). CV measurements of the symmetric cells were performed on a CHI 760E electrochemical workstation from -1 V to +1 V at a scan rate of 3 mV s^{-1}. To measure Li_2S nucleation and deposition, CR2025 cells were assembled using lithium foils as the anodes and the same TaPcCo-MWCNT/CNF (or pristine CNF) electrodes used in the symmetric cells as the cathodes. The electrolyte was a 0.2M Li_2S_8 solution that was prepared by reacting sulfur and Li_2S (molar ratio 7:1) at 65 °C for 24 hours in DME/DOL (1:1, v/v) containing 1M LiTFSI. The cells were first galvanostatically discharged to 2.08 V at 0.1 mA. The voltage was then switched to 2.07 V and held constantly for the measurement of the Li_2S nucleation and deposition current. For the assembly of Li-S full cells, TaPcCo-MWCNT/CNF/S (or CNF/S) was mixed with Super P carbon black and PVDF binder at the mass ratio of 8:1:1 in NMP and slurry coated on Al foils to form the cathodes. Cathodes with areal sulfur loadings of 2. 5 and 7 mg cm^{-2} were prepared. All prepared

cathodes were vacuum dried at 50 °C for 12 hours and pouched into 12 mm diameter discs before use. CR2025 cells were assembled in an Ar-filled glove box. Rolled lithium foils with the thickness of 0.15 mm and purity of 99.9% was into 14 mm diameter discs to serve as anodes. Celgard 2400 polypropylene membranes with the diameter of 16 mm were used as the separators. The electrolyte was 1 M LiTFSI with 2 wt% $LiNO_3$ in DME/DOL (1:1, v/v). The E/S ratio was 10 μL mg^{-1} for the 2 mg cm^{-2} cathodes and E/S ratios of 4, 6 and 8 μL mg^{-1} were tested on the 5 mg cm^{-2} cathodes to obtain the optimized value for the higher sulfur loadings. CV measurements on Li-S full cells were performed on a CHI 760E electrochemical workstation between 1.6 V and 2.9 V at scanning rates of 0.1, 0.2, 0.5 and 1 mV s^{-1}. Li-ion diffusion coefficient D_{Li^+} was calculated using the Randles−Sevcik equation:

$$I_p = (2.65 \times 10^5) n^{1.5} S {D_{Li^+}}^{0.5} \Delta C_{Li^+} v^{0.5} \quad (1)$$

Where I_p denotes the peak current , n is the electron transfer number (2 for Li-S batteries), S represents the geometric area of the electrode (1.13 cm^2) and v is the scan rate. I_p *vs* $v^{0.5}$ was plotted and the corresponding D_{Li^+} was calculated from the curve slops. Galvanostatic charge/discharge tests were performed on a NEWARE BTS4000 battery test system between the cut-off voltages of 1.60 V and 2.65 V at 25 °C. All specific capacities were calculated based on the mass of sulfur. EIS measurements were carried out on a CHI 760E electrochemical workstation at a frequency range from 100 kHz to 0.01 Hz with a 5 mV AC amplitude.

Theoretical calculations: DFT calculations of the Li_2S_6 adsorption geometries and energies on TaPcCo-MWCNT were performed using the Vienna Ab-initio Simulation Package.[2, 3] The projector augmented wave (PAW) potentials were used to describe the electron-ion interactions and the Predew-Burke-Ernzerhor functional with generalized gradient approximation was

employed to describe the electron exchange and correlation energy.[4, 5] A cut-off energy of 480 eV was utilized for the plane wave basis set and a 3×3×1 k-point mesh was used for the Brillouin zone sampling. A Li_2S_6 molecule was placed at approximately 4 Å away from the TaPcCo-MWCNT model and the adsorption geometry optimization was carried out until the convergence threshold of 0.02 eV $Å^{-1}$ was reached. The binding energy (E_b) is defined as

$$E_b=E_{total}-E_{sub}-E_{ps} \quad (2)$$

where E_{total} is the total energy of the binding system, E_{sub} is the energy of the optimized binding substrate and E_{ps} is the energy of the Li_2S_6 adsorbate. The spin-polarized DFT simulations were performed with the $Dmol^3$ package to calculate the sulfur reduction free energy and the energy barrier of Li_2S decomposition. The double numeric plus polarization (DNP) basis set with the global orbital cutoff of 4.5 Å was used in the local atomic orbital basis set. The convergence criteria for the self-consistent field (SCF) was set to be 10^{-6}. The structures were optimized until the maximum force is lower than 0.002 Ha/Å. The linear synchronous transit/quadratic synchronous transit (LST/QST) and nudged elastic band (NEB) tools were used to determine the minimum energy path and energy barriers. In the climbing image nudged elastic band calculations of Li_2S decomposition, 4 images for transition states were obtained between the initial and final states.

References

[1] Bevington PR, Robinson DK. Data reduction and error analysis for the physical sciences. 3rd ed. McGraw-Hill. 2003.
[2] G. Kresse, J. Hafner, Phys. Rev. B **1993**,*48*, 13115.
[3] G. Kresse, J. Furthmuller, Phys. Rev. B **1996**,*54*, 11169.
[4] P. E. Blochl, Phys. Rev. B **1994**, *50*, 17953.
[5] J. P. Perdew, K. Burke, M. Ernzerhof, Phys. Rev. Lett. **1996**, *77*, 3865.

Supporting Figures

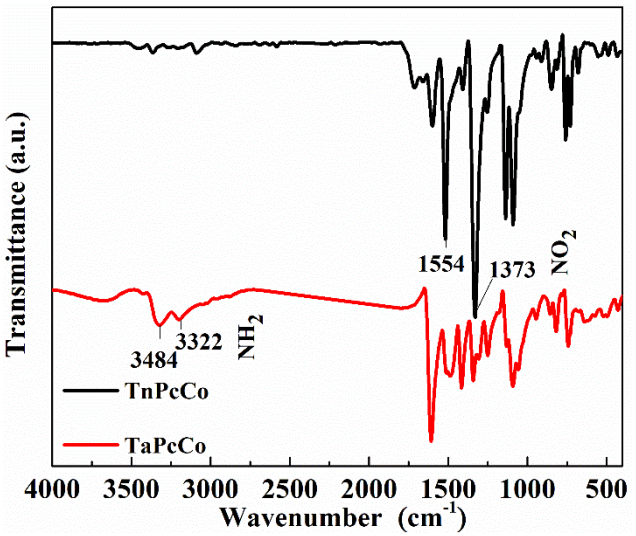

Figure S1. FTIR spectra of TnPcCo and TaPcCo. The characteristic peaks at 1554 cm^{-1} and 1373 cm^{-1} on TnPcCo can be assigned to the stretching vibrations of substituent nitro groups on the Pc rings. TnPcCo was transformed to TaPcCo by reducing the nitro groups to amino groups using sodium sulphide. Peaks at 3493 $cm^{-1}$and 3497 cm^{-1} on TaPcCo represent the stretching vibrations of the newly-formed amino groups.

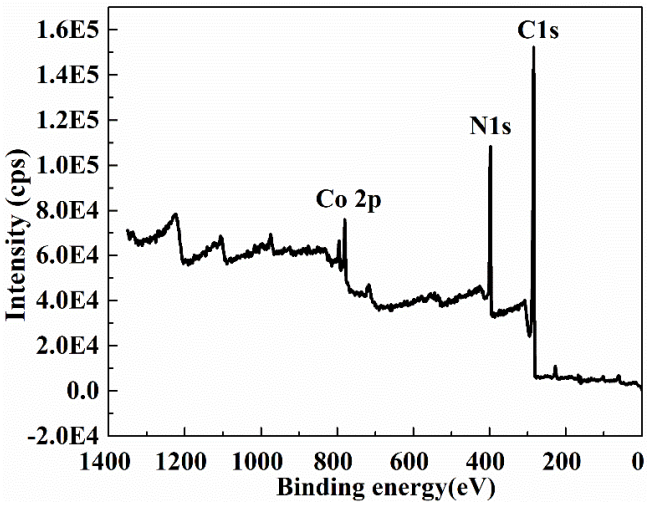

Figure S2. XPS survey spectrum of TaPcCo-MWCNT.

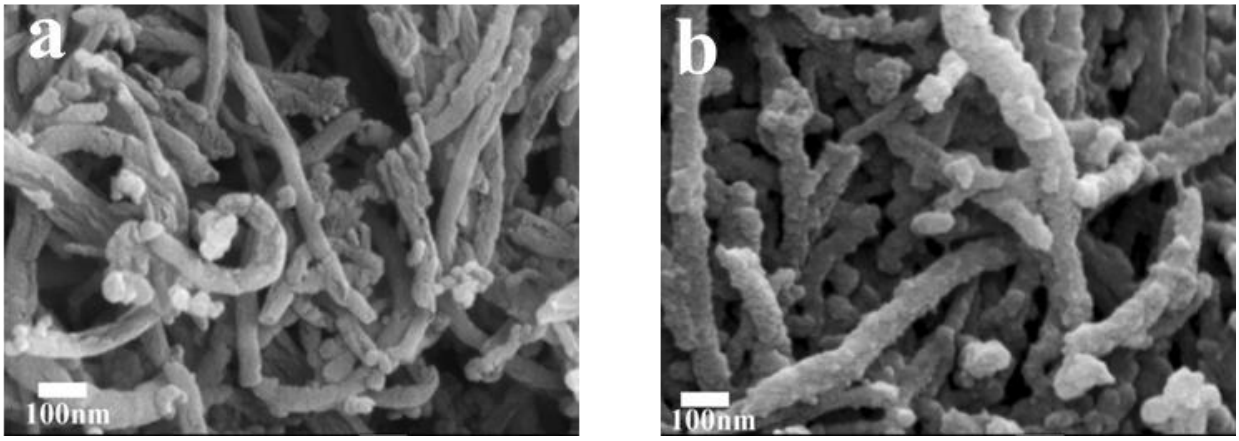

Figure S3. SEM morphologies of a) F-MWCNT and b) TaPcCo-MWCNT.

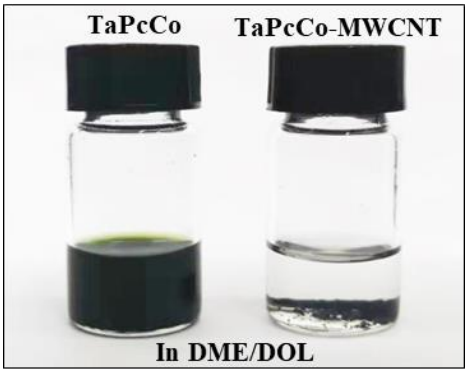

Figure S4. Dissolution of pure TaPcCo in the DME/DOL solvent as compared with no leakage of TaPcCo from TaPcCo-MWCNT to the electrolyte due to covalent binding to the MWCNT skeleton.

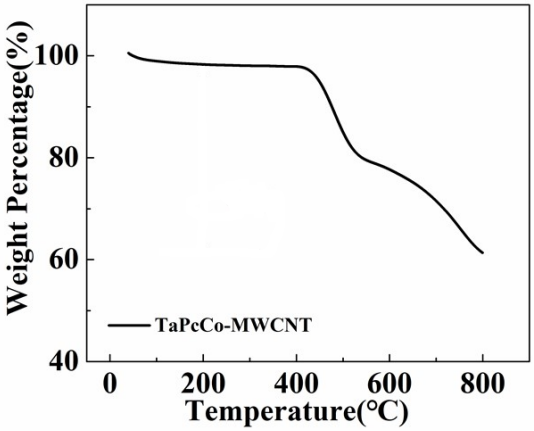

Figure S5. TGA profile of TaPcCo-MWCNT. The sample was heated under N_2 atmosphere from 25 ℃ to 800 ℃

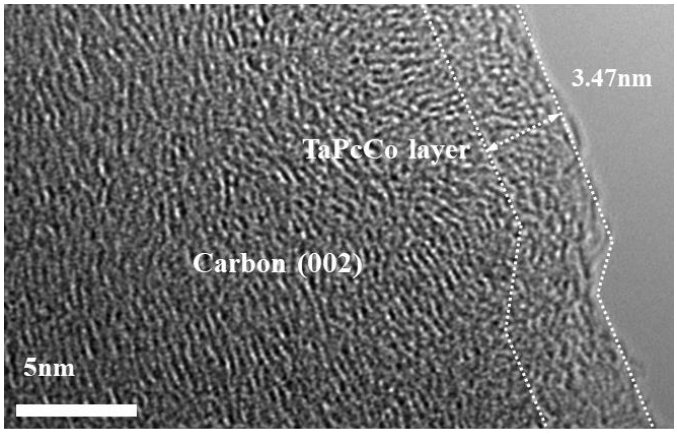

Figure S6. HRTEM image on the edge of TaPcCo-MWCNT.

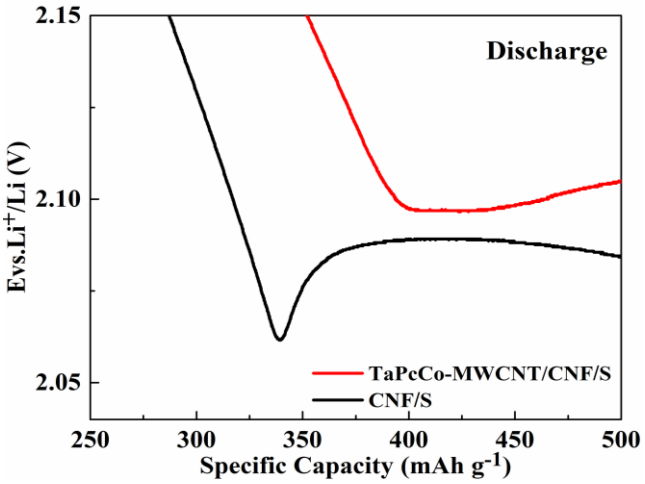

Figure S7. 0.2 C discharge profiles of TaPcCo-MWCNT/CNF/S and CNF/S onset to the second voltage plateau.

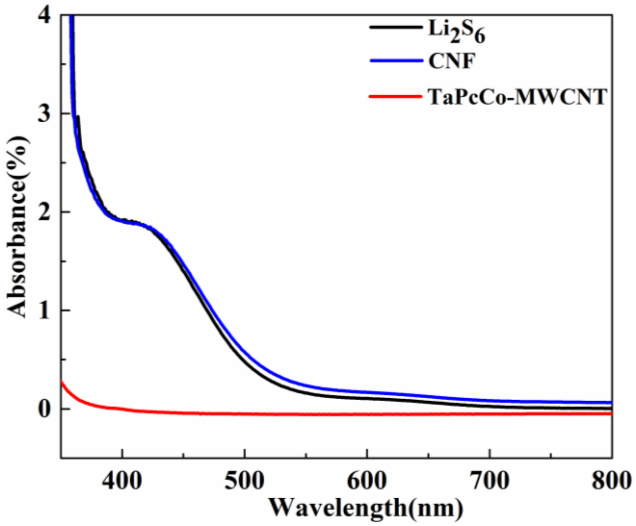

Figure S8. UV-vis spectra of Li_2S_6 solutions before and after soaking with CNF and TaPcCo-MWCNT.

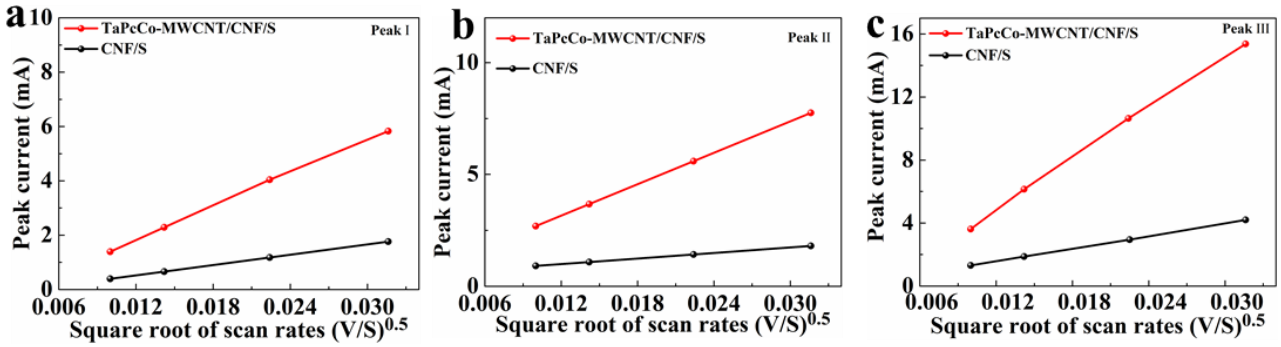

Figure S9. Plots of peak currents *vs* the square root of scan rates derived from the CV profiles in Figure 4c-d for a) peak I, b) peak II and c) peak III.

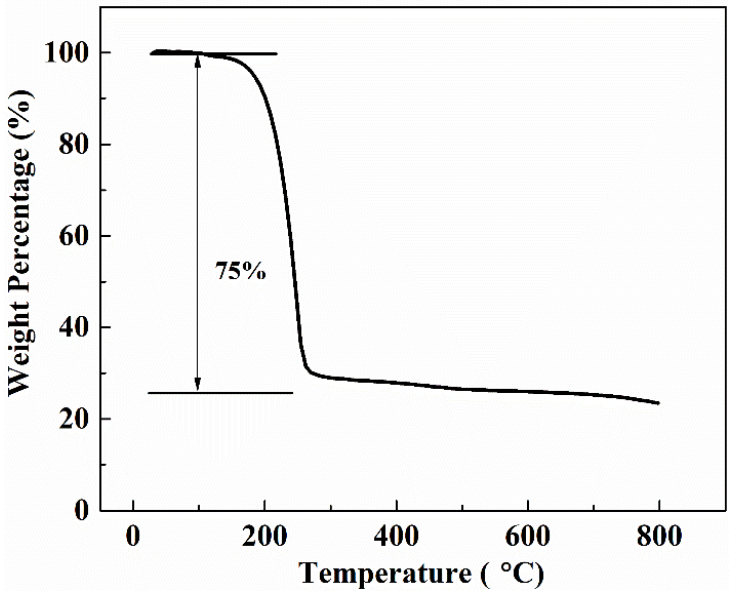

Figure S10. TGA profile of TaPcCo-MWCNT/CNF/S. The sample was heated under N_2 atmosphere from 25 ℃ to 800 ℃, and the weight-loss of 75 wt% corresponds to the content of sulfur in the composite.

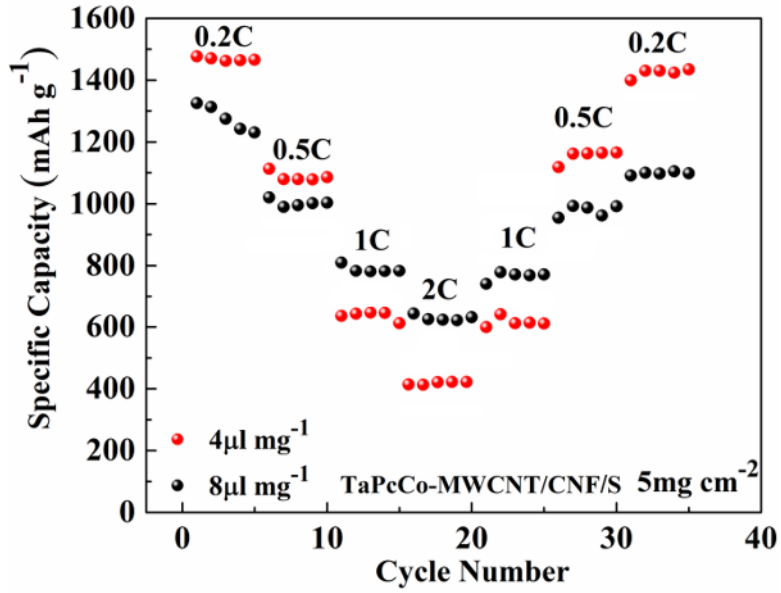

Figure S11. High-rate capability of TaPcCo-MWCNT/CNF/S with the E/S ratio of 4μl mg^{-2} and 8μl mg^{-2} at the areal sulfur loading of 5 mg cm^{-2}.

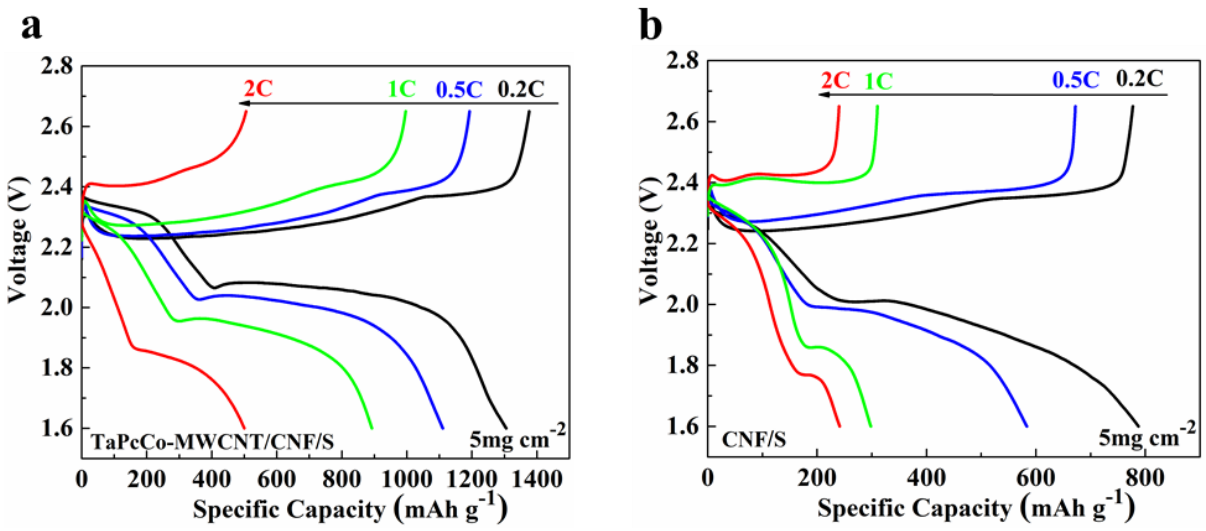

Figure S12. Galvanostatic charge/discharge profiles of a) TaPcCo-MWCNT/CNF/S and b) CNF/S at various C rates under the areal sulfur loading of 5 mg cm^{-2}.

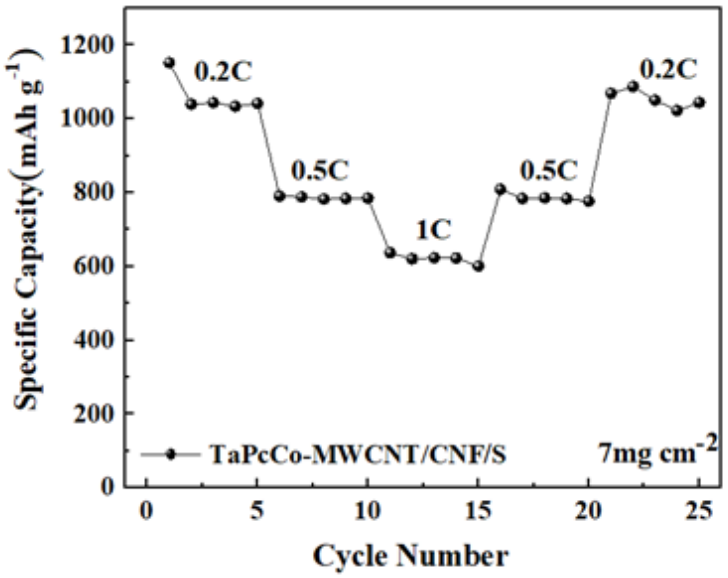

Figure S13. High-rate capability of TaPcCo-MWCNT/CNF/S at the areal sulfur loading of 7 mg cm^{-2}.

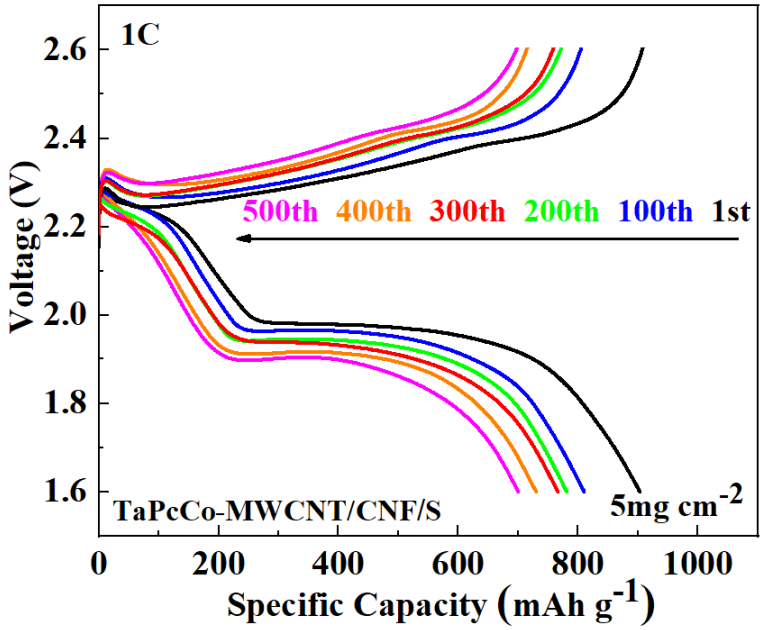

Figure S14. Galvanostatic charge/discharge profiles of TaPcCo-MWCNT/CNF/S from various charge/discharge cycles at 1C and 5 mg cm^{-2} areal sulfur loading.

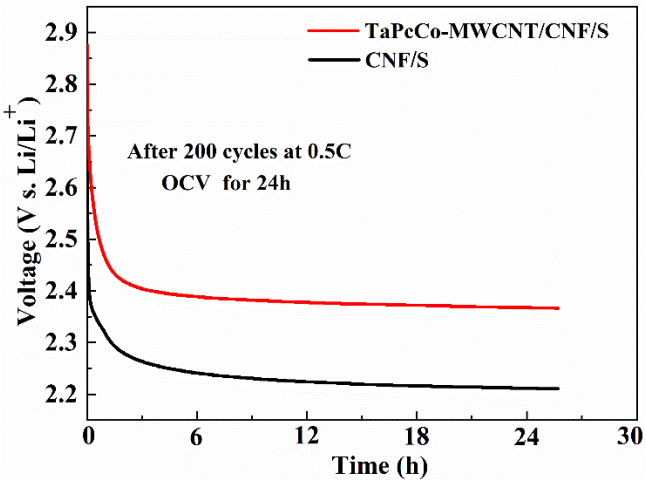

Figure S15. Open circuit voltage (OCV) profiles of the 5mg cm^{-2} sulfur loading fully-charged Li-S cells with TaPcCo-MWCNT/CNF/S and CNF/S after 200 cycles charge/discharge tests at 0.5C.

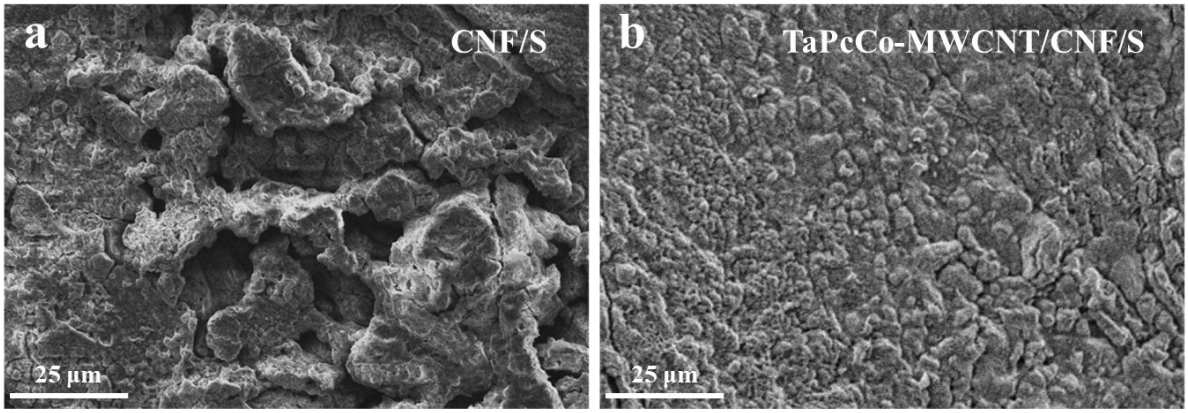

Figure S16. SEM morphologies of Li anodes cycled at 0.5C fro 200 cycled with a) CNF/S and b) TaPcCo-MWCNT/CNF/S cathodes.

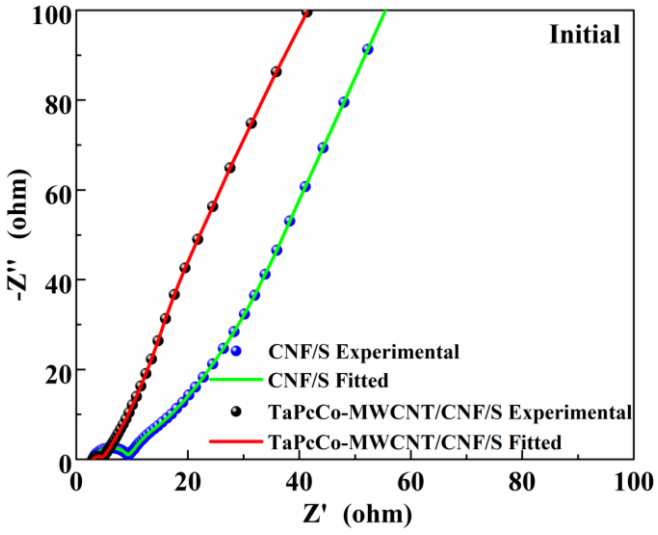

Figure S17. EIS Nyquist plots of uncycled cells with TaPcCo-MWCNT/CNF/S and CNF/S.

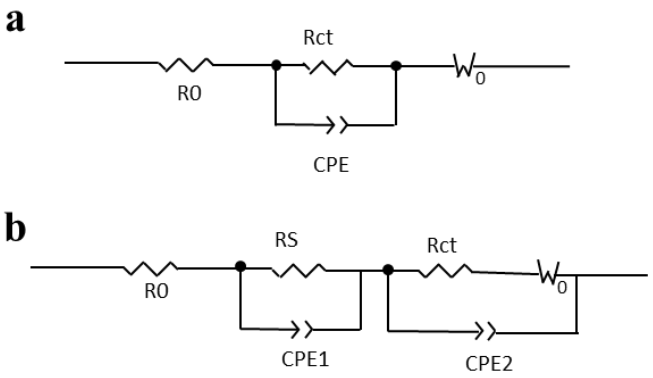

Figure S18. ESI equivalent circuit models used for a) uncycled and b) cycled cells.

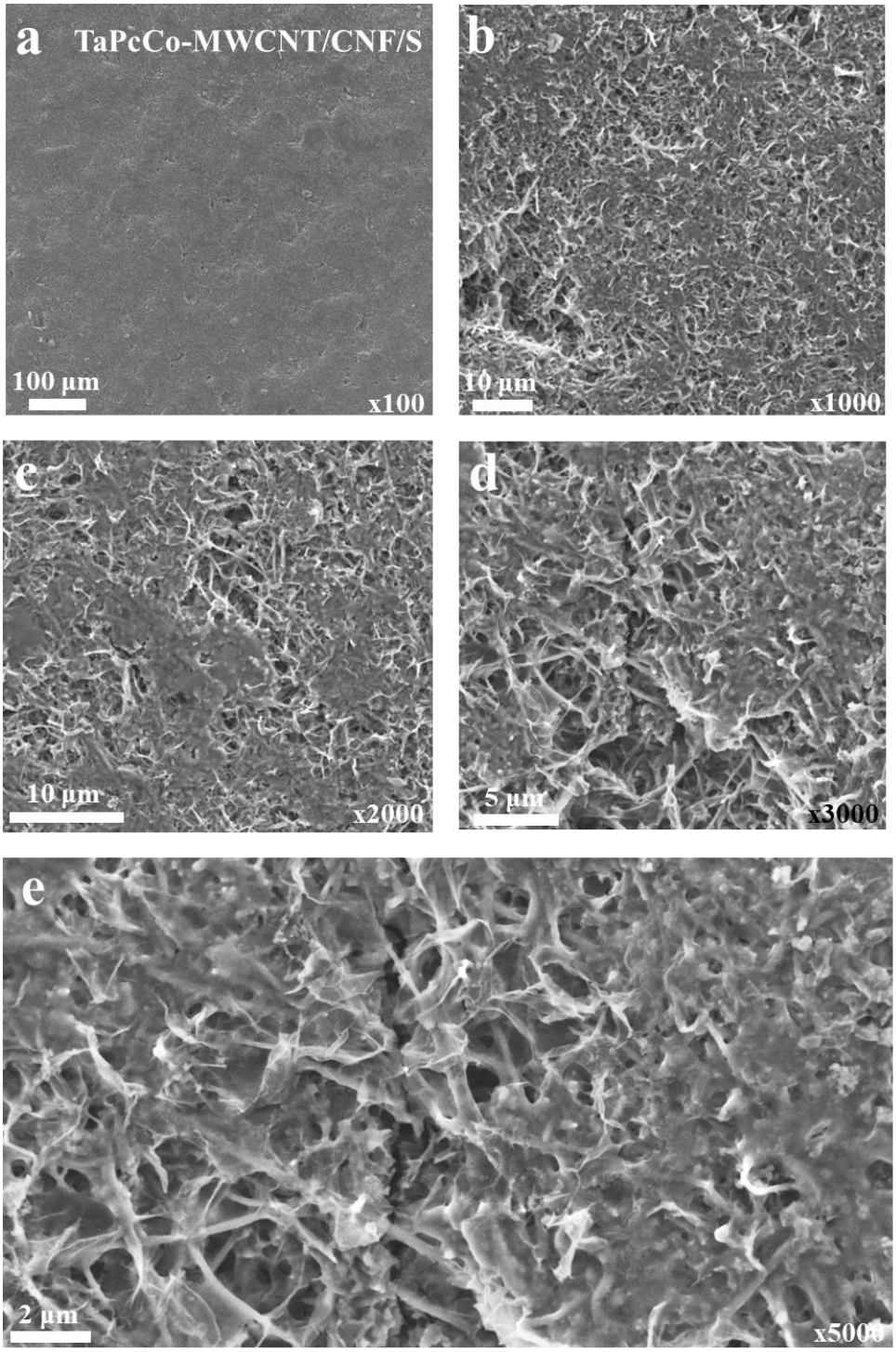

Figure S19. SEM morphologies of the cathode with TaPcCo-MWCNT/CNF/S after 200 charge/discharge cycles in the discharged state taken at the magnifications of a) x100, b) 1000, c) 2000, d) 3000 and e) 5000.

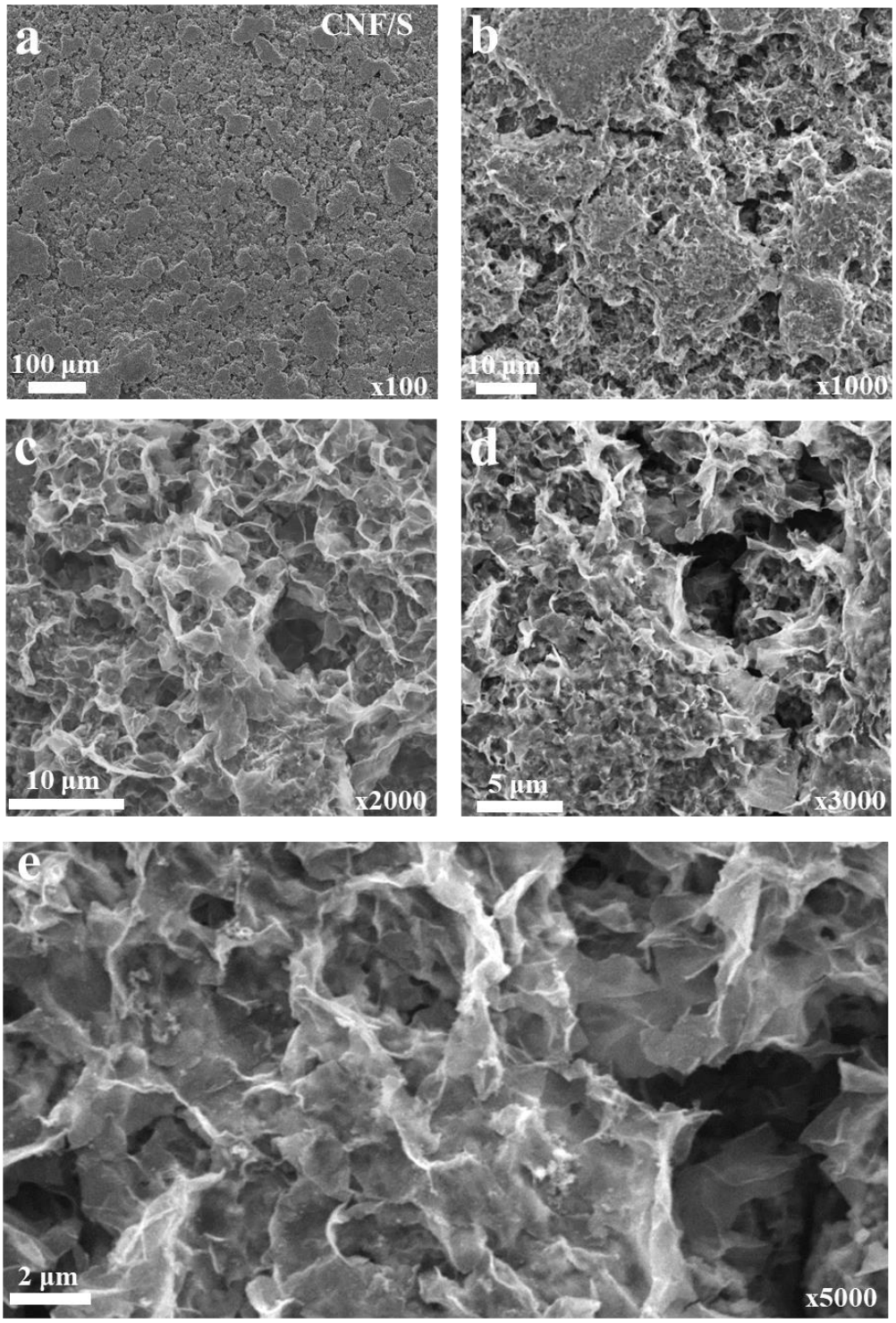

Figure S20. SEM morphologies of the cathode with CNF/S after 200 charge/discharge cycles in the discharged state taken at the magnifications of a) x100, b) 1000, c) 2000, d) 3000 and e) 5000.

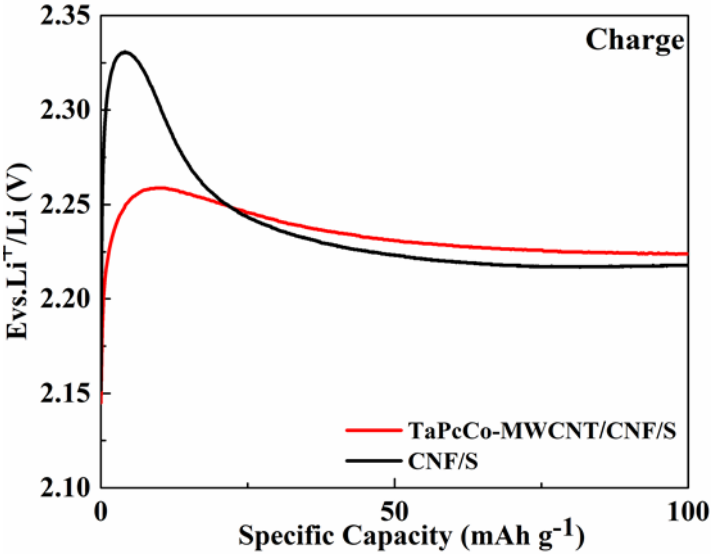

Figure S21. 0.2 C charge profiles of TaPcCo-MWCNT/CNF/S and CNF/S onset to the first voltage plateau.

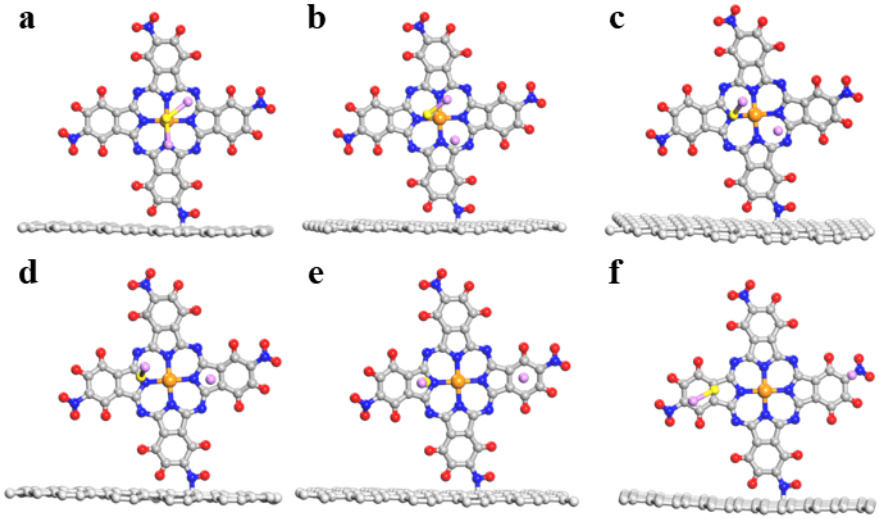

Figure S22. DFT models of the Li_2S decomposition process on TaPcCo-carbon showing a) the initial state, b-e) four transition states, and f) the final state.

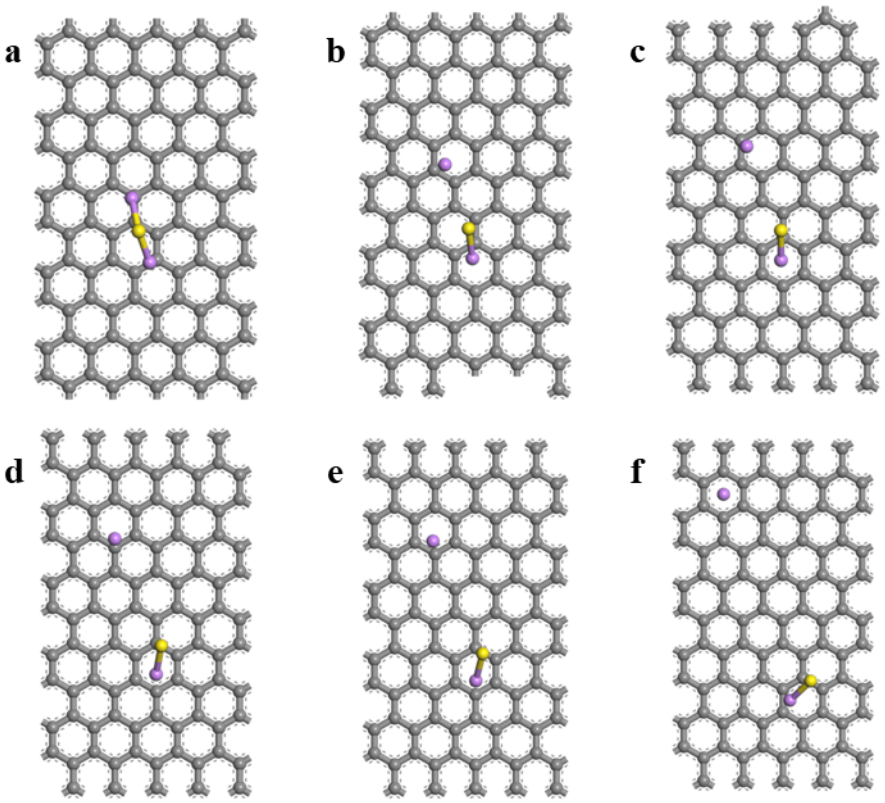

Figure S23. DFT models of the Li_2S decomposition process on pristine graphitic surface showing a) the initial state, b-e) four transition states, and f) the final state.

Supporting Tables

Table S1. Li-ion diffusion coefficient D_{Li^+} for TaPcCo-MWCNT/CNF/S and CNF/S.

Sample	D_{Li^+} (I)* [$cm^2\ s^{-1}$]	D_{Li^+} (II) * [$cm^2\ s^{-1}$]	D_{Li^+} (III) * [$cm^2\ s^{-1}$]
TaPcCo-MWCNT/CNF/S	5.05×10^{-8}	5.67×10^{-8}	1.34×10^{-7}
CNF/S	1.55×10^{-8}	1.08×10^{-8}	1.55×10^{-8}

*calculated form Peak I, II and III from the CV profiles in Figure 4c-d.

Table S2. ESI fitted parameters for TaPcCo-MWCNT/CNF/S and CNF/S.

Sample	Cycle	R_0 [Ω]	R_{ct} [Ω]	R_s [Ω]	W_0 [Ω]
TaPcCo-MWCNT/CNF/S	0	3.12	1.60	-	23.65
	200	5.24	2.43	4.41	11.56
CNF/S	0	3.21	5.64	-	37.88
	200	5.37	8.88	10.89	21.74